ABSTRACT

PERKINS, JAMES ROBERT. Raman Spectroscopy – in situ Characterization of Growth and Surface Processes. (Under the direction of Robert J. Nemanich.)

The goal of this thesis is to expand on the usefulness of Raman spectroscopy as an in situ probe to aid in the growth and implementation of electronic, optical, and biodetection materials. We accomplish this goal by developing two diverse optical characterization projects. In the first project, an autoclave similar to those used in solvothermal growth which has been outfitted with an optical window is used to collect vibrational spectra of solvents and mineralizers commonly used in the ammonothermal growth of gallium nitride. Secondly, novel silver nanowires created by ferroelectric lithography are evaluated by surface enhanced micro-Raman spectroscopy for use as surface enhanced substrates for low detection limit or single molecule bio-detectors.

Raman spectroscopy is already a widely accepted method to characterize and identify a wide variety of materials. Vibrational spectra can yield much information on the presence of chemical species as well as information regarding the phase and interactive properties. Because Raman spectroscopy is a generally non-intrusive technique it is ideal for analysis of hazardous or far-from-ambient liquids, gases, or solids. This technique is used in situ to characterize crystal growth and surface enhanced photochemistry.

The phenomenon of Surface Enhanced Raman Spectroscopy (SERS) has been observed in many systems but some fundamental understanding is still lacking and the technique has been slow to transition from the laboratory to the industry. Aggregated colloids and lithographically created islands have shown the best success as reproducible

substrates for SERS detection. These techniques, however, lack control over shape, size, and position of the metal nanoparticles which leave them reliant on hotspots. Because of the potential for control of the position of aggregates, ferroelectric lithographically created silver nanowires are evaluated as a potential SERS substrate using pyridine, benzoic acid, and Rhodamine 6g. Surface enhancement from these samples varies periodically as excitation light is scanned perpendicular to the wires. The periodicity, however, has the frequency of the positive domains where carbon laser damage is preferentially created.

There is a current need for homoepitaxial substrates for gallium nitride devices including light emitting diodes, transistors, and laser diodes. Ammonothermal growth is a promising technique for creating bulk single crystalline GaN, but questions remain concerning the intermediates of reactions in supercritical Ammonia. Neat ammonia and water are monitored by Raman spectroscopy from room temperature to 500 ºC and 20 kpsi with both UV and visible excitation. In both systems, the amount of hydrogen bonding, which can be determined by O-H and N-H stretch frequency shifts, decreases with increasing temperature. In supercritical ammonia, the degree of Fermi resonance between the ν_1 and $2\nu_4$ modes decreases linearly with temperature while a minimum in pyramidal height of the NH_3 molecule is reached at moderate pressures. Binary solutions of sodium azide and ammonia are investigated to temperatures which allow observation of the breakdown of the azides. The pressure and N_2 Raman signal increase as the azide decomposes to sodium amide and N_2 and H_2 process gasses. The rate of decrease of the Raman signal of the azide increases as the reaction proceeds suggesting that the reaction rate is proportional to the pressure. The Fermi resonance, hydrogen bonding, and pyramidal height parameters were not affected by the presence of the azide.

Raman Spectroscopy – in situ Characterization of Growth and Surface Processes

by

James Robert Perkins

A dissertation submitted to the Graduate Faculty of
North Carolina State University
in partial fulfillment of the
requirements for the degree of
Doctor of Philosophy

Physics

Raleigh, North Carolina

2007

APPROVED BY:

Dr. Robert J. Nemanich Co-Chair of Advisory Committee	Dr. Zlatko Sitar Co-Chair of Advisory Committee
Dr. J. E. (Jack) Rowe	Dr. Dave E. Aspnes
Dr. Hans D. Hallen	

DEDICATION

To my Parents,

Rick and Jenny,

whose unconditional support, expert advice, and patient understanding

not only made this work possible but also inspired me to undertake it.

BIOGRAPHY

James Perkins was born and raised in the Asheville, North Carolina area. He graduated from T.C. Roberson High School in 1997. He received his Bachelor of Arts in physics with a minor in mathematics from North Carolina State University in 2002. After teaching undergraduate physics laboratories for a year, he joined the graduate program at his alma mater.

ACKNOWLEDGEMENTS

The author wishes to thank all the members of the Surface Science Laboratory at NC State. Joe Tedesco, Jacquie Hanson, Jen Huening, Simon Stampe, Sarah Earl, Jacob Garguilo, Franz Koeck, Joshua Smith, Luke Bilbro, Eugene Bryan, Yingjie Tang, Jiyoung Choung, Matt Zeman, and Anderson Sunda-Meya were helpful coworkers, kind friends, and 'water cooler collaborators' of this work. Also in that category are several members of the WideBandGaps Laboratory including Ramon Collazo, Rafi Dalmau, Xianglin Li, and Seiji Mita. The faculty of the NC State physics department and in particular my committee members deserve thanks for their efforts in this work and for making me feel like a peer while still keeping me in check. Jenny Allen, CJ Hathorne, and Jan Jackson were so friendly and approachable that it made me look forward to paperwork. Michael Callahan of AFRL was one of many very helpful collaborators from the Bulk Nitrides MURI. The Materials Science Precision Engineering machine shop, and in particular Rick Lamy, showed incredible patience with my design blunders and cocktail napkin sketches. Thanks go to Eric Lambers of the University of Florida MIAC for SAM characterization. If you ever need anything brazed, contact Doug Rich at Omley Industries; he is a pleasure to work with. I would like to thank all my friends and family for being patient with me over these last four years. My sisters, Jewel and Maggie, and brother, Patrick, have been a constant reminder to work hard to set a good example; I thank them for their love. I owe Erin Franz for the joy she brings into my life and thank her for being by my side. And finally, I thank my parents for whom this work is dedicated and to whom any success I might enjoy is owed.

TABLE OF CONTENTS

List of Figures vi

1. Introduction 1
   1.1 Fundamentals of Raman Spectroscopy 1
   1.2 Surface Enhanced Raman Scattering 7
   References 9

2. Raman Spectroscopy of Solvents and Mineralizers Used in Solvothermal Growth 14
   2.1 Introduction 15
   2.2 Experimental 17
   2.3 Results and Discussion 20
      2.3.1 UV Raman of Supercritical Water 20
      2.3.2 UV Raman of Supercritical Ammonia 22
      2.3.3 Visible Raman of Supercritical Ammonia 24
      2.3.4 Visible Raman of Sodium Azide in Ammonia 26
   2.4 Conclusions 29
   References 30

3. Surface Enhanced Raman Spectroscopy of Silver Nanostructures grown by Ferroelectric Lithography 50
   3.1 Introduction 51
   3.2 Experimental 53
   3.3 Results and Discussion 55
      3.3.1 Spatial Periodic Surface Enhancement from Silver on PPLN 55
      3.3.2 Laser Damage 57
   3.4 Conclusions 61
   References 63

4. Epilogue 77
   4.1 Ammonthermal Future Work 77
   4.2 SERS Future Work 79

LIST OF FIGURES

Figure 1.1 Schematic of the quantized vibrational, rotational, and electronic energy levels of a molecule 11
Figure 1.2 Demonstration of the Raman selection rules for linear and non-linear A-B-A molecules 12
Figure 1.3 Schematic of the Rayleigh, Stokes Raman, and anti-Stokes Raman vibrational modes of CCl_4 13
Figure 2.1 Schematic of the high temperature, high pressure autoclave 32
Figure 2.2 UV Raman scattering from supercritical water 33
Figure 2.3 Temperature-pressure relationship for supercritical water 34
Figure 2.4 ν_{max} and FWHM of the O-H stretch of supercrtical water 35
Figure 2.5 UV Raman of liquid ammonia at 20 C and 135 psi 36
Figure 2.6 UV Raman of ammonia between 23 and 244 C and 135 to 7300 psi 37
Figure 2.7 Temperature-pressure relationship for supercritical ammonia 38
Figure 2.8 Log ammonia ν_1 molar intensity vs. temperature 39
Figure 2.9 Visible Raman of supercritical ammonia to 350 C and 13 kpsi 40
Figure 2.10 $\nu_{1,max}$ and FWHM of the N-H stretch of supercrtical ammonia 41
Figure 2.11 Temperature dependence of anharmonic force constant, K_{144} 42
Figure 2.12 Intensity of NH_3 ν_1 band as a function of pressure 43
Figure 2.13 Raman spectra of solid and solvated NaN_3 44
Figure 2.14 Temperature and pressure changes in time during azide decomposition 45
Figure 2.15 Azide and nitrogen Raman intensity and pressure vs. time 46
Figure 2.16 Schematic of location of precipitates after autoclave evacuation 47
Figure 2.17 Temperature dependence of K_{144} in azide-ammonia system 48
Figure 2.18 Temperature-pressure relationship for azide-ammonia system 49
Figure 3.1 Schematic of micro-Raman sampling stage 65
Figure 3.2 AFM and PFM of silver nanowires created by ferroelectric lithography 66
Figure 3.3 AFM height profile of selective deposition on domain boundary and positive domain 67
Figure 3.4 SERS of 10^{-4} M pyridine on lithium niobate 68
Figure 3.5 Spatially periodic enhancement of pyridine ring breathing mode intensity 69
Figure 3.6 AFM and PFM of laser damaged region 70
Figure 3.7 SEM of silver nanowires on lithium niobate 71
Figure 3.8 Auger spectroscopy of lithium niobate with silver nanowires 72
Figure 3.9 Scanning auger microscopy on silver nanowires on PPLN 73
Figure 3.10 SERS of laser damaged region 74
Figure 3.11 Benzoic acid SERS intensity as a function of time 75
Figure 3.12 Effect of laser power on pyridine SERS intensity 76

1. Introduction

Raman Spectroscopy is a staple of the modern laboratory. The theory is easy to understand, the equipment is simple and relatively inexpensive, the information gleaned from the technique is invaluable, and the technique is extremely versatile. The goal of this study is to expand on the versatility of Raman spectroscopy by citing two diverse studies. Each of the chapters in the work outlines a current topic of interest which is still growing. Raman spectroscopy can help these topics not only in understanding but in commercial success.

1.1 Fundamentals of Raman Spectroscopy

Since the prediction of inelastic light scattering by A. Smekal [1] in 1923 through the first observation of Raman scattering by C. V. Raman and K. S. Krishnan [2] in 1928 to the present, the technique of Raman Spectroscopy continues to develop and prove to be a staple of materials characterization techniques. As a versatile, non-intrusive probe of the vibrational and rotational spectra of molecules, Raman Spectroscopy is an invaluable method for identification of materials and a probe of the phase and intra- and intermolecular properties.

This chapter discusses many of the basic properties and principles of the Raman scattering phenomenon and advantages and limitations of Raman spectroscopy. A classical derivation of inelastic light scattering illustrates the frequency dependence of scattered light and is supplemented by a partial quantum mechanical treatment in order to derive scattering intensities. Some examples of the applications of and equipment used in

Raman Spectroscopy are outlined and special techniques are briefly discussed. In the second half of the chapter, one of these special techniques, Surface Enhanced Raman Spectroscopy, is discussed in detail.

Within the quantum mechanical description of Raman scattering, the photon interacts with material to change its vibrational and/or rotational state. For scattering from a solid, this interaction may be understood as the creation or annihilation of a phonon, a quantized vibration of atoms in a rigid crystal lattice. The incident light excites the material to a virtual, disallowed state. The scattered photon's energy can be divided into three possible categories, greater than, less than, or equal to the incident energy. These changes in energy of the photon are identical to the differences in energy of the initial and final vibrational states as is illustrated in Figure 2.1. The elastically scattered light is usually termed the Rayleigh scattered light. That which has lost energy (and thereby raised the vibrational state of the molecule or created a phonon) is denoted as the Stokes shifted light. Light which has gained energy (and lowered the vibrational state of the molecule or annihilated a phonon) is the Anti-Stokes shifted light.

In order to better demonstrate frequency dependence of Raman scattering using classical electromagnetic theory, imagine a space fixed N atom molecule as classical oscillator with 3N-6 (3N-5 for linear molecules) normal modes of vibration. Each mode, with normal coordinate, q_i, can be viewed as a classical oscillation with frequency ν_i, determined by nuclear coordinates and bond force constants

$$q_i = q_{i0}\cos(2\pi\nu_i t)$$

The electric field of the incident light, E, will induce a polarization, P, in the molecule according to $P = \alpha E$ where α is the polarizability. It is necessary to assume that

the wavelength of the incident light is much larger than the molecule so that the electric field is approximately constant over the whole molecule at a given time.

Expanding the polarizability in a Taylor series about the nuclear displacements, q_i, and asserting the approximation that the amplitude of vibration, q_0, is small so that higher order terms can be dropped yields a polarization caused by an electric field, E,

$$P = \alpha E \approx \left[\alpha_0 + \left(\frac{\partial \alpha}{\partial q_i} \right)_0 q_i \right] E \, .$$

Adding the time dependence of the incident electric field of light of frequency ν_0

$$E = E_0 \cos(2\pi \nu_0 t)$$

yields

$$P = \alpha_0 E_0 \cos(2\pi \nu_0) + \left(\frac{\partial \alpha}{\partial q_i} \right)_0 E_0 q_0 \cos(2\pi \nu_0 t) \cos(2\pi \nu_i t)$$

$$= \alpha_0 E_0 \cos(2\pi \nu_0) + \frac{1}{2} \left(\frac{\partial \alpha}{\partial q_i} \right)_0 E_0 q_0 \{ \cos[2\pi (\nu_0 - \nu_i) t] + \cos[2\pi (\nu_0 + \nu_i) t] \}$$

This represents an oscillating dipole which will radiate electromagnetic energy at three frequencies. The term with unchanged frequency ν_0 represents the Rayleigh scattering component. The other two terms account for the Stokes Raman scattering of frequency $(\nu_0 - \nu_i)$, and anti-Stokes Raman scattering of frequency $(\nu_0 + \nu_i)$.

Even this simple, classical derivation illustrates many facts about Raman scattering besides the frequency dependence. The Raman scattering amplitude is proportional to the derivative of the polarizability with normal coordinate. This condition illustrates the selection rule for vibrational Raman scattering. If the derivative of the polarizability with

respect to the normal coordinate of vibration evaluated at the equilibrium position is zero, then that vibration is normally not Raman active. For example, consider the linear and non-linear A-B-A molecules depicted in Figure 2.2. The q_1 mode of the linear molecule and all three modes of non-linear molecule will be Raman active. Because we assumed mechanical and electrical harmonicity, this classical derivation does not predict overtones and combination tones. However, this assumption is too restrictive and in general overtones and combination tones are present albeit typically much weaker than the fundamental modes. Fermi resonance between overtones, combination tones, or fundamentals tends to increase the intensity of both resonant modes and shift their energies toward each other.

Although scattering cross sections depend on many factors and can vary by several orders of magnitude, the Rayleigh scattered light is typically a thousand times less intense than the incident radiation, and the Stokes Raman scattered light is again a thousand times less intense than the Rayleigh. The intensity ratio between the Stokes and Anti-Stokes scattering events is a Boltzmann distribution function of the temperature and is proportional to the probability of finding the molecule in an excited vibrational state at a given temperature. Figure 2.3 shows a schematic of the Stokes, anti-Stokes and Rayleigh lines of CCl_4 spectrum to demonstrate the relative intensities of these bands. The scattering cross section, $\frac{d\sigma}{d\Omega}$, of an oscillating dipole is given by [3]

$$\frac{d\sigma}{d\Omega} = \frac{d\Phi/d\Omega}{\mathrm{I}_{incident}} = \frac{\pi^2 \nu^4 P_0}{c^2 E_0^2} \sin^2\theta .$$

Inserting the quantum mechanical polarization transition moments [4] into P_0 yields a scattered intensity of a Raman band that is linearly proportional to incident laser intensity,

number of molecules in the sampling area, and the fourth power of the frequency, $(\nu_0 \pm \nu_{if})^4$

$$I = \frac{64\pi^2}{3c^2} \mathrm{I}_{incident} (\nu_0 \pm \nu_{if})^4 \mathrm{N}(\alpha_{if}^2)$$

where (α_{if}^2) are the squares of the polarizability transition moments which depend on scattering and collection geometries and the polarizability of the molecule. These polarizability transition moments are complex and require full knowledge of the wavefunctions of all electronic and vibrational states of the molecule. However, by evaluating the symmetries of these wavefunctions, Group theory can predict the polarization dependencies of the vibrational energy levels and selection rules for molecules or crystals. [5]

Because it is applicable to materials in solid, liquid, and vapor phases, the applications of Raman spectroscopy span several fields. The most obvious is the non-intrusive identification of organic and inorganic species for which the unique, vibrational 'fingerprint' of the molecule is known. Because the Raman scattering intensity is proportional to the number of molecules in the sampling area relative concentrations of solutes can be learned. If special care is taken and the Raman scattering cross sections are known then absolute concentrations and densities are derivable. [6] The inverse application in structural chemistry is of course also possible; Raman spectra and polarization analysis (or orientation dependence of scattering intensities in crystalline structures) can be used to deduce the symmetry and structure of a sample. Information on the effects of temperature,

pressure, stress, and environment on a molecule or solid is gained by measuring the changes in shape, energy, and intensity of Raman bands.[3]

Special Raman techniques continue to develop which are tailored to the particular applications. Many of these new techniques are possible due to the continuing improvement of laser sources, focusing and collection optics, high resolution wavelength dispersers, and sensitive detectors. Resonance Raman Spectroscopy and Coherent anti-Stokes Spectroscopy are made possible in a variety of samples by the invention of tunable IR and visible lasers. Raman microscopy and imaging are the result of quick Charged Coupled Device (CCD) detectors and the use of a microscope as a sampling device.

The Resonance Raman effect is important because of its possible implications in Surface Enhanced Raman Spectroscopy. [7] Resonance Raman occurs when the excitation energy is close or equal to an electronic excited state. Resonance Raman cross sections can be as much as five orders of magnitude larger than non-resonant cross sections. The first order perturbation of the transition polarizability tensor component is given by [8]

$$\left[\vec{\alpha}_{xy}\right]_{FG} = \frac{1}{\hbar}\sum_{R}\left(\frac{\langle F|P_y|R\rangle\langle R|P_x|G\rangle}{\omega_{GR}-\omega_0-i\Gamma_R}+\frac{\langle R|P_y|G\rangle\langle F|P_x|R\rangle}{\omega_{RF}-\omega_0-i\Gamma_R}\right)$$

where $|F\rangle$ and $|G\rangle$ are the final and initial (ground) state and Γ is the band width of the electronic state (the damping constant). As the laser frequency, ω_0 , approaches one of the electronic excited frequencies, $\omega_{GR}=\omega_G-\omega_R$, the first term in the summation will become resonant. Resonant Raman spectroscopy can be used for low concentration detection or to isolate individual Raman spectral features from a part of a large molecule.

The Resonance Raman effect also plays a role in Surface Enhanced Raman scattering which is discussed in detail in the next section.

1.2 Surface Enhanced Raman Scattering

While studying Raman scattering of pyridine adsorbed on electrochemically roughened silver surfaces in 1974, Fleischmann et al. [9] observed an anomalously large scattering cross section. Since this discovery the field of Surface Enhanced Raman Scattering (SERS) has blossomed to include a variety of substrates and hundreds of adsorbates. Because Raman scattering cross sections are small, SERS has made possible detection of Raman signals that were thought to be much too weak to observe including sub-monolayer and single molecule detection. While much progress has been made in understanding and taking advantage of this phenomenon, some controversy still exists over the mechanism of enhancement and improvement of substrates is necessary for this technique to move beyond the laboratory.

Two mechanisms, which are likely to both contribute to the effect, are at the root of the theory of surface enhancement. The first is an electromagnetic enhancement of the electric field near sub-wavelength conducting structures caused by surface plasmon resonance. The second, thought to be the weaker effect, is an induced charge transfer complex between the adsorbate and metal which can enhance Raman scattering intensity through the Resonance Raman effect.

The electromagnetic effect relies on two factors 1) exciting with a wavelength that is at or near a surface plasmon resonance and 2) suitable roughness features that allow the

surface plasmon to radiate electromagnetic energy. The surface plasmon resonance will be a function of not only the electronic properties of the metallic surface but also of the surface rougness. Near a metal surface of nanoscale roughness the incident electric field of the laser can excite a surface plasmon which can radiate electromagnetic energy in the near field that is many times stronger than incident field. If an adsorbate is on or near this surface, the enhanced field will increase the Raman scattered intensity by the same factor. In fact, the Raman scattered fields will also be enhanced by the surface in the same manor as the incident field. This secondary enhancement is applicable because Raman shifts are typically smaller than the plasmon resonance envelope.

Consider the polarizability of a small (sub-wavelength) metal sphere [10]

$$\alpha = \frac{\varepsilon(\omega) - \varepsilon_0}{\varepsilon(\omega) + 2\varepsilon_0} R^3 .$$

The plasmon resonance frequency, ω_R will satisfy the equation [7]

$$0 = \mathrm{Re}\,\varepsilon(\omega_R) + 2\varepsilon_0$$

and will have an enhancement factor proportional to $\mathrm{Im}\,\varepsilon(\omega_R)^{-4}$. This is only an instructive example, however, because actual SERS measurements are almost always made from aggregates of nanoparticles or surfaces with nanoscale roughness. Between nanoparticles the induced charges caused by the incident field can create a capacitive field which increases as the inter-particle distance decreases, especially in cases where the incident light is polarized along the interpaticle axis. [11]

The dependence of plasmon resonance on the real and imaginary parts of the wavelength dependent dielectric constant makes certain metals such as silver, gold, and copper ideal for SERS substrates.[12] Enhancement will be governed by choice of

wavelength depending on the size, shape, and substrate material. Although roughness features can be created by a number of methods there is a theoretical limit on the size of the features ranging from approximately 5 to 100 nm. [10]

References

1) A. Smekal, Naturwissenschaften, **11**, 873 (1923).

2) C. V. Raman and K. S. Krishanan, Nature, **121**, 501, (1928).

3) D.A. Long, *Raman Spectroscopy* (McGraw-Hill Inc., London, 1977).

4) L. A. Woodward, in *Raman Spectroscopy: Theory and Practice,* edited by H. A. Szymanski (Plenum Press, New York, 1967) p.1.

5) G. Herzberg, *Molecular Spectra and Molecular Structure: II. Infrared and Raman Spectra* (D. Van Nostrand Company Inc., Princeton NJ, 1945).

6) H. W. Schrotter and H. W. Klockner, in *Raman Spectroscopy of Gases and Liquids*, edited by A. Weber (Springer –Verlag, Berlin, 1979) p.123.

7) H. Metiu, in *Surface Enhanced Raman Scattering*, edited by R. K. Chang and T.E. Furtak (Plenum Press, New York, 1982) p.1.

8) D.L. Rousseau, J.M. Friedman, and P.F. Williams, in *Raman Spectroscopy of Gases and Liquids*, edited by A. Weber (Springer –Verlag, Berlin, 1979) p.203.

9) M. Fleischman, P.J. Hendra, and A.J. McQuillan, Chem. Phys. Lett. **26**, 123 (1974).

10) M. Moskovits, in *Surface Enhanced Raman Scattering: Physics and Applications*, edited by K. Kneipp, M. Moskovits, H. Kneipp (Springer-Verlag, Berlin, 2006) p.1.

11) P.K. Aravind, A. Nitzan, H. Metiu: Surf. Sci. **110**, 189 (1981)

12) M. Moskovits, Rev. Mod. Phys. **57**, 783 (1985).

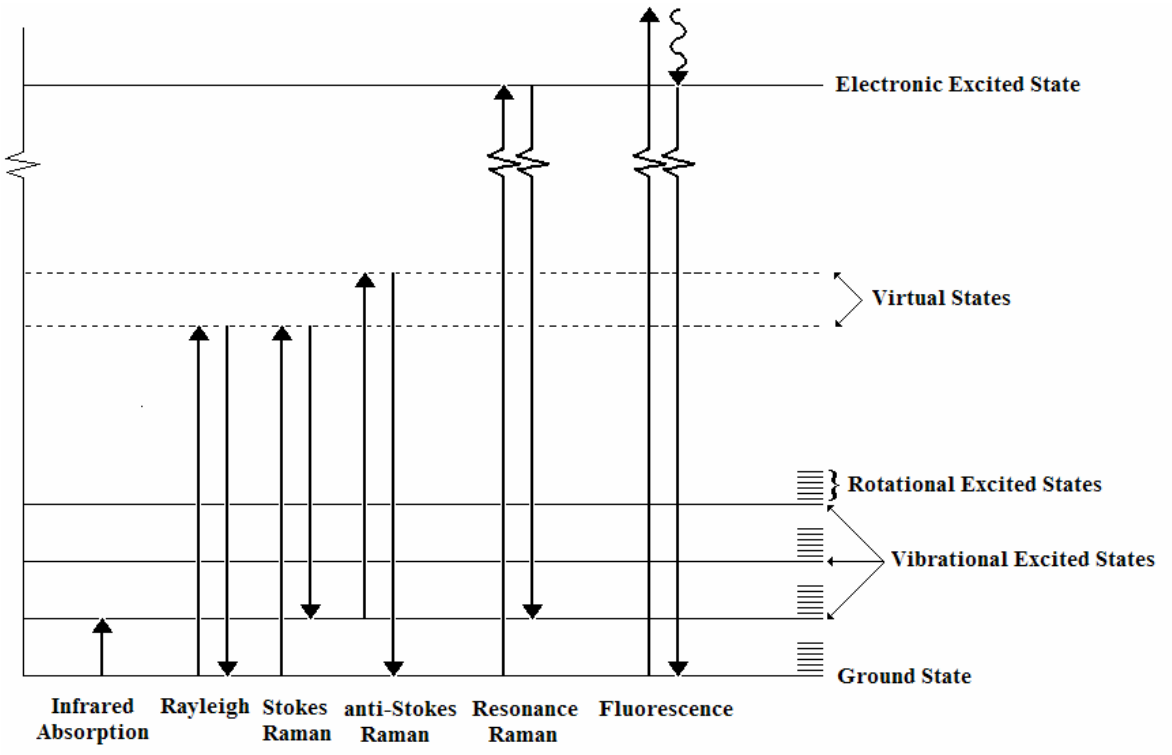

Figure 2.1 Schematic of the quantized vibrational, rotational, and electronic energy levels of a molecule.

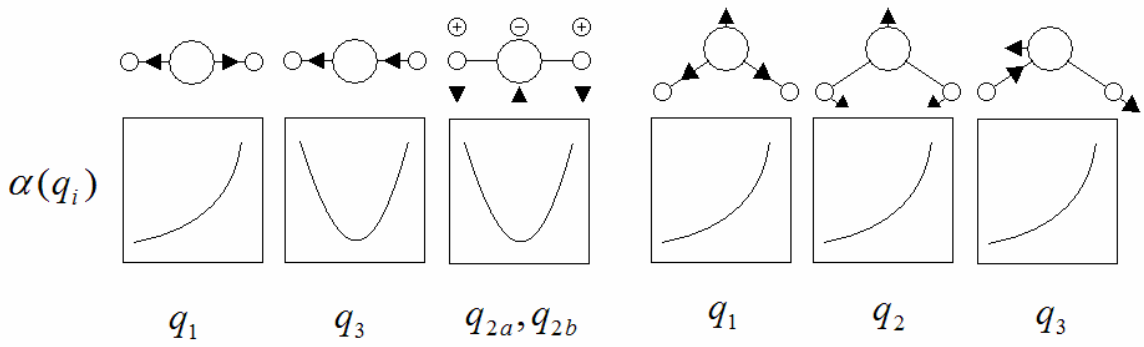

Figure 2.2 Demonstration of the Raman Selection Rules for linear and non-linear A-B-A molecules. For the q_3 and doubly degenerate q_2 modes of the linear molecule, the derivative of the polarizability, α, with respect normal coordinate, q_i, at equilibrium will be zero, and those modes are therefore Raman inactive.

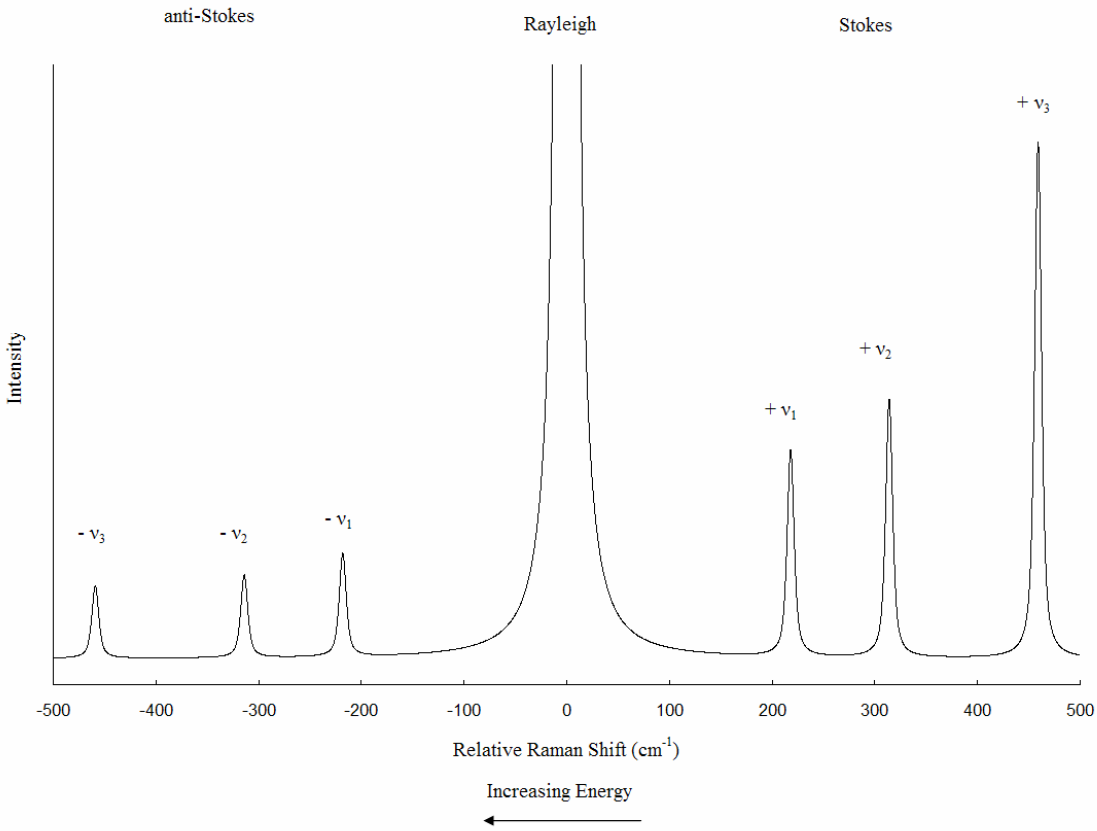

Figure 2.3 Schematic of the Rayleigh, Stokes Raman, and anti-Stokes Raman vibrational modes of CCl_4.

2. UV and Visible Raman Spectroscopy of Solvents and Mineralizers Used in Solvothermal Growth

ABSTRACT

Raman Spectroscopy is used to probe the vibrational spectra of supercritical water, ammonia, and binary solutions of sodium azide and ammonia. Supercritical ammonia is used as a solvent in the ammonothermal growth of group III nitrides, particularly gallium nitride. While the usefulness of the ammonothermal technique is growing rapidly, many of the mechanisms and properties of supercritical solvents and solutions including azide and amide mineralizers are still unknown. An autoclave similar to those used in growth has been fitted with a sapphire window to allow optical characterization. Raman spectroscopy offers a unique opportunity to identify intermediates in growth reactions as well as provide information on concentration, solubility, and transport properties. UV and visible Raman spectra of neat water and ammonia have been collected at up to 500 ºC and 20 kpsi at a variety of fill densities. The amount of hydrogen bonding in both systems decreases rapidly below the critical temperature and slowly above this temperature. In supercritical ammonia the degree of Fermi resonance between the ν_1 and $2\nu_4$ modes decreases linearly with temperature while the pyramidal height of the NH_3 molecule has a local minimum at moderate pressures. Visible Raman spectra of binary solutions of sodium azide and ammonia are measured up to and above the decomposition temperature of the azide. The Raman signal intensities of the azide and nitrogen molecules are monitored during the decomposition and suggest that the rate of decomposition increases with increasing pressure. The hydrogen bonding, Fermi resonance, and pyramidal height parameters of ammonia were not affected by the presence of the azide.

2.1 Introduction

Gallium nitride and its alloys are important materials for electronic and elctro-optical devices such as laser diodes, light emitting diodes, [1] and transistors.[2] Most current GaN devices are created on sapphire or SiC substrates. The lattice mismatch between the nitride and substrate causes defects which limit the performance and lifetime of these devices.[3] There is therefore a need for bulk single crystal gallium nitride substrates.

Because of the high melting temperature and dissociation pressure of GaN, bulk crystals are difficult to grow. [4] One promising method of achieving bulk growth is the ammonothermal process where supercritical ammonia is used as a solvent. [5] Supercritical solvents are advantageous because they provide increased and adjustable solubility of reaction products, display transport properties similar to those of the gas phase, and can often increase reaction rates.[6]

Similar to the hydrothermal synthesis of α-quartz, ammonothermal synthesis uses a mineralizer to attack the powder GaN or metallic gallium feedstock to form a soluble gallium intermediate.[7] By use of a temperature gradient the soluble species is transported to the crystallization site (usually containing a GaN seed grown by hydride vapor phase epitaxy) where a state of supersaturation is achieved. While much success has been made with the ammonothermal growth of gallium nitride, [8] the process still suffers from a number of deficiencies, including impurity incorporation, ammonia breakdown, free nucleation on autoclave walls, and a lack of knowledge of important factors such as solubilities, transport properties, and reaction intermediates.[9]

Raman spectroscopy is an ideal tool to analyze this system in situ by identifying reactants, providing relative concentrations, and shedding light on solubility and transport properties.[6]

In this study, Raman spectra of supercritical water were collected in order to test the optical, mechanical, and thermal capabilities of the device; however, this data proved valuable academically later on because of the many similarities with ammonia, particularly the effects of hydrogen bonding. While UV Raman of ammonia proved difficult due to temperature dependent UV absorption, visible spectra were obtained in good agreement with results from the literature. [10] Different from most previously published results that analyzed isobaric and isothermal systems, [11] this work utilizes an isochoric cell most similar to those used in actual synthesis. In the final section, the binary mixture of ammonia and sodium azide was measured.

2.2 Experimental

A high pressure autoclave with an optical window was designed and built specifically for these studies and is shown schematically in Figure 2.1 The autoclave body and window housing were constructed from Inconel Alloy 718 which was chosen for its low iron content and thermal and mechanical durability. Cylindrical sapphire windows were used due to their hardness, chemical inertness, strength, and optical transmission in the UV and visible. The sapphire windows were brazed into the inconel housings using a silver active braze alloy. Initial experiments showed that gold braze alloys showed significant weight loss in ammonia at elevated temperatures which led to using silver braze joints. For fills containing sodium azide, the silver braze joints were nickel plated because silver showed signs of deterioration possibly due to the formation of silver azide. Autoclave Engineers High Pressure Series tubing, fittings, fill valve, safety relief valve, and pressure detector were connected to the autoclave by a custom inconel adaptor. The total internal volume of the autoclave was 10.4 ml while the plumbing volume was only 3.2 ml.

The autoclave was heated by a custom band heater capable of 600 ºC. The plumbing was heated separately by tape heaters. Two thermocouples were used for temperature sensing; one was placed between the band heater and autoclave wall, and the other was held between the heating tape and plumbing. Because of the temperature limitations of the fill and the relief valves and the pressure transducer, the plumbing could be heated to a maximum of 150 ºC. Because the thermocouple was outside of the

autoclave, measured temperatures (and those reported here) overestimate the temperature of the sampled ammonia. Pressure measurements were consistently lower than expected due possibly to the effect of heating the strain gauge.

The autoclave was filled by condensing liquid NH_3 into the autoclave which was submersed in a dry ice/isopropanol bath at approximately -78 ºC. A mass flow controller measured the amount of ammonia added. For fills with sodium azide, a measured amount of powder azide is put in the cell before it is sealed and evacuated. Fill percents used in this paper are determined by the formula,

$$fill\% = \frac{m_{ammonia}}{\rho V}$$

where ρ is the density of liquid ammonia at -78 C and 20 psi (these fill percents do not take into account the volume displaced by sodium azide when it was used).

For UV Raman measurements, a Spex 1877 spectrometer with a CCD detector was used. A Coherent Innova FReD doubled argon ion UV laser operating at 244 nm was used for excitation. The laser power at the sample was approximately 10 mW. Visible excitation was obtained with 514 nm excitation from a Coherent Innova-90 argon ion laser. At the sample, visible excitation measured approximately 30 mW. Visible spectra were collected using only the spectrometer stage from a Jobin Yvon HR 640 monochrometer equipped with a Princeton Instruments 1028 pixel CCD. For visible Raman a laser filter was used before the sample to eliminate plasma lines and a 514 nm notch filter was used after the sample to block Rayleigh scattering. For both UV and visible Raman, 180 degree backscattering geometry was required in order to use only one window. No polarization analysis was performed in either the UV or visible.

Collected spectra were corrected by subtraction of the dark background and manual removal of atmospheric peaks. Fluorescence from the sapphire window was subtracted from visible Raman spectra, however, this fluorescence was many times stronger than the Raman signal and occasional interfered with data collection. Sapphire fluorescence is strongly temperature dependent and can be eliminated by using higher quality sapphire. Jandel Scientific's Peakfit was used for fitting and deconvolution.

2.3 Results and Discussion

2.3.1 UV Raman of Supercritical Water

Our study began with water instead of ammonia for several reasons, namely that it was easier and safer to fill, and it was possible to achieve high densities. UV excitation was chosen because of the ν^4 dependence on Raman scattering intensity. As hydrogen bonded liquids, ammonia and water share many characteristics and therefore water made an ideal substance to test and calibrate the system. They also have similar thermodynamic properties; the critical point of water is 374 ºC and 3200 psi while that of ammonia is 132 ºC and 1643 psi.

Water molecules belong to the C_{2v} space group which normally has three Raman active modes. Water in the liquid and supercritical states display the ν_1 symmetric stretch mode which has a cross section large enough for detection without intense excitation.[12] Figure 2.2 shows the Raman spectrum of water in the O-H stretch region for a 50% water fill at temperatures from 23 to 593 ºC. The corresponding pressure-temperature relation for this fill is displayed in Figure 2.3. The temperature and pressure have to be corrected for nonlinearity effects caused by heating the pressure strain gauge. The O-H stretch region includes the ν_1 symmetric O-H stretch band at 3657 cm^{-1} which is broadened and blue-shifted by a network of hydrogen bonding. Previous authors analyzing spectra obtained with visible excitation have deconvoluted this region into five Gaussian peaks which represent O-H stretches of H_2O dimers and higher order conjugates.[13] The five peak

fit was unsuitable for our spectra and only the peak position, ν_{max} , and full width at half maximum (FWHM) of the entire band were considered.[12] As the temperature and pressure increase, the position of the maximum increases while the half width decreases. Both of these effects are related to reduction in the amount of hydrogen bonding. [12] These shifts are shown graphically in Figure 2.4 in a manner similar to that of Ikushima et al.[12] Between 200 and 300 ºC, both of these factors change rapidly. This corresponds to the temperature range over which the density of the liquid begins to increase rapidly. Under isobaric conditions, Ikushima et al. observed the greatest rate of change in half-width and ν_{max} at the critical temperature.

The intensity of broad liquid water band decreases suddenly at 234 ºC due to the level of water in the cell falling below the laser sampling area. The unperturbed steam, H_2O ν_1 monomer, peak at 3657 cm^{-1} can be seen as a shoulder at this temperature. Note that the intensity scales between the top and bottom graphs are not the same but that the general trend is decreasing intensity with increasing temperature.

There is an exception to this trend near the critical temperature. The intensity is lowest near the critical point due to critical opalescence.[14] Near the critical point scattering is increased by density fluctuations typical of a second order phase transition. Many of these trends hold for ammonia which is investigated in the following sections.

2.3.2 UV Raman of Supercritical Ammonia

Ammonia belongs to the C_{3v} space group which has four Raman active modes. The UV Raman spectrum of liquid ammonia at room temperature is shown in Figure 2.5. At room temperature, all four modes can be observed. Additionally, the 2nd overtone of the doubly degenerate ν_4 asymmetric bending mode is relatively intense at all temperatures and pressures due to being in Fermi Resonance with ν_1 symmetric stretch.[15] Fermi resonance tends to increase the scattering cross section of both modes as well as shift their frequencies toward their average. The ν_1 symmetric stretch region of ammonia is also broadened by hydrogen bonded ammonia dimers similar to the ν_1 symmetric stretch region of water.[16] Also similar to water, above standard temperatures and pressures, the intensities of the ν_2, ν_3, and ν_4 modes decrease rapidly with increasing temperature making the N-H stretch region of the most interest in this study. The ν_1 and $2\nu_4$ modes of NH_3 should remain strong scatterers and are easily observed at supercritical conditions with visible excitation.[17]

As expected, the ν_1 mode is observed to increase in frequency and decrease in half width with increasing temperature (Figure 2.6). This observation has been attributed to the breaking of the ammonia dimer hydrogen bonds. [16] Unexpected and detrimental to UV Raman studies of ammonia was the exponential and uniform decrease of the intensity of the entire spectrum. Temperature-Pressure data (Figure 2.7) showed that ammonia was not leaking out of the cell, and previous experiments with water assured that the sapphire windows were still transparent at these temperatures.

A UV absorption band corresponding to the ($^1A_2 \leftarrow {}^1A_1$) electronic transition at 180-230 nm at room temperature is known to increase in absorbancy and red shift with increasing temperature.[19] Because the sampling area was a finite distance (~2mm) past the window, absorbance would attenuate both the incident and scattered light according to Beer's Law. Figure 2.8 shows that the intensity of the ν_1 band decreases exponentially with increasing temperature for several fill percents. Intensities in this plot were normalized to each other by setting the total integrated intensity of the room temperature band for each fill percent to unity; they were also normalized by density in accordance with the method of Buback et al.[17]

2.3.3 Visible Raman of Supercritical Ammonia

Figure 3.9 shows visible Raman of the ammonia symmetric stretch region over three different temperature regions. These spectra compare favorably to previous Raman studies on supercritical ammonia. 4 Several factors, which are well documented for condensed ammonia in the isobaric and isothermal system, are monitored in the neat, isochoric cell for comparison with the system with solute included in the cell. These factors include thermodynamic sensitivity of hydrogen bonding, the degree of Fermi resonance between the ν_1 and $2\nu_4$ bands, and the pyramidal deformation of the NH_3 molecule.

Similar to the water spectrum, the amount of hydrogen bonding can be seen in the width and blue-shift of the ν_1 region. In water the hydrogen bonding network is more complex, and so the width and position are stronger functions of temperature and density in the water system. In Figure 2.10, the position and width of the ammonia ν_1 are plotted as a function of temperature in the same fashion of the water spectrum in Figure 2.4.

The degree of Fermi resonance between the ν_1 and $2\nu_4$ is measured by the strength of the anharmonic force constant, K_{144}.[19] It has been shown that the degree of Fermi resonance decreases with temperature due to the shift of ν_1 toward the unperturbed vapor frequency. The anharmonic force constant can be calculated by the formula

$$K_{144} = \Delta\sqrt{2R}/(R+1)$$

where R is the ratio of intensity of the ν_1 and 2 ν_4 peaks and Δ is the frequency separation of the Fermi doublet components. In Figure 2.11 values of K_{144} are evaluated for a 65% NH_3 fill and are compared to tabulated data from previous authors.[19]

At low pressures, the pyramidal height of the NH_3 molecule is decreased by interaction of the nitrogen lone pair electrons with neighboring molecules. Electron charge density transfer from a hydrogen bonded neighbor into the N-H bond will increase repulsion between the N-H bonds thereby decreasing pyramidal height. However, at higher pressures the pyramidal height reverses this trend and increases. Because polar molecules are able to be packed closely, the ammonia molecules will increase their pyramidal height to become more polar at high densities. There is therefore a minimum pyramidal height which occurs at some moderate to high pressure.[17] The intensity of the ν_1 stretch is an indicator of the pyramidal height because the polarizability of the molecule will be affected by its shape. The intensity of the ν_1 peak as a function of pressure is shown in Figure 2.12. It can be seen that a maximum of intensity (and hence a minimum in pyramidal height) is seen at 10 kpsi.

2.3.4 Visible Raman of Ammonia/Sodium Azide

NaN_3 was chosen as a mineralizer for a number of reasons: 1) it is readily soluble in NH_3 at ambient temperatures, 2) it is less reactive than $NaNH_2$ and can be handled and filled without the need for a glove box (for growth, this also means less incorporated O_2 and H_2O), 3) it has a lower decomposition temperature than KN_3 and could therefore be observed at temperatures that would allow the window to survive. Growth runs have utilized potassium amides and azides more than their sodium counterparts due to the fact that KNH_2 is much more soluble than $NaNH_2$.[9] Figure 2.13 shows the Raman spectrum of solid sodium azide and azide dissolved in NH_3 at two temperatures. The two features in the spectra of azide in solution correspond to the solvated (1328 cm^{-1}) and free (1320 cm^{-1} at room temperature, 1355 cm^{-1} at 275 ºC) ν_1 modes. The "free" mode is highly temperature dependent and quickly moves to higher wavenumbers as the temperature increases.[20]

At moderate temperatures the azide was completely undetectable by Raman, this may be due to the increase in sapphire fluorescence over this temperature range. At high temperatures, the azide Raman signal is again detectable.

Above 295 ºC, the pressure in the cell slowly increases at constant temperature. The azide is known to decompose at 275 ºC according to the formula[9]

$$NaN_3 \rightarrow Na + N_2.$$

Pressure increases are also due to the subsequent formation of sodium amide

$$Na + NH_3 \rightarrow NaNH_2 + H_2.$$

Figure 2.14 shows the changes in temperature and pressure over time near the decomposition temperature.

Above 275 ºC, N_2 can be detected in the cell. The intensity of the N_2 line at 2326 cm^{-1} increases slowly until 300 ºC was reached. This increase in N_2 signal is attributed to concentration increases as the aforementioned reactions proceed. The azide signal also decreases as the reaction proceeds as expected. Figure 2.15 shows the pressure and N_2 and N_3^- Raman signal intensities as functions of time, at a constant temperature of 300 ºC. The rate of decline of the azide Raman signal presumably indicates the progression of the reaction. Assuming that the azide Raman signal is independent of pressure, we can conclude the reaction rate increases with increasing pressure. Spectra obtained from 4000 to 5000 cm^{-1} did not show the H_2 Raman signal. Hydrogen is produced at one third the rate of N_2 and, even though it has a larger scattering cross section, it is less soluble in NH_3.

After the reaction had completed, and the cell cooled to room temperature a large overpressure of N_2 (or H_2) remained in the cell. Evacuating and opening the autoclave revealed a hard white solid on the side of the autoclave. The autoclave is filled and evacuated in a vertical position, but spectroscopy and heating occur while the cell is oriented horizontally as is shown schematically in Figure 3.16. This white solid, therefore, came out of solution during the spectroscopy measurements, either when the cell was cooled to room temperature or possibly as it was formed at elevated temperatures.

Upon opening the autoclave, the white solid reacted with atmosphere to form a highly basic liquid. The solid reacted energetically when mixed with water. All of these are indicative of the solid being the expected $NaNH_2$ (which reacts with ambient H_2O to form the highly basic NaOH and NH_3).

The $NaNH_2$ signal was not detected during the spectroscopy measurement. This is attributed to one of two factors (or both): 1) $NaNH_2$ is only sparingly soluble in NH_3 even at elevated temperatures and may have precipitated out of the sampled solution, 2) the Raman spectrum of NH_2 will have its strongest bands in the same region as the NH_3 N-H stretch which may obscure by the NH_2 signal.

The inclusion of sodium azide does not seem to strongly affect the NH_3 hydrogen bonding or pyramidal deformation. This can be quantized by comparing the temperature dependence of the NH_3 anharmonic force constant from section 2.3.3 (Figure 3.17). The P-V-T relationship between the neat ammonia system and the NH_3-NaN_3 system is shown if Figure 3.18. As reported by Callahan[9] et al. the pressures in the NH_3-azide system are lower than those of the neat ammonia system.

2.4 Conclusions

The specially designed autoclave and window withstood temperatures and pressures used in the dissolution zone of ammonothermal GaN synthesis. The Raman spectra of relevent process gasses and reactants have been detected at supercritical temperatures. Also the Raman spectrum of neat supercritical ammonia at several fill percents has been collected. Measurement of neat ammonia spectra as a function of temperature and pressure will prove as an important baseline to determine solvent-solute effects which can affect transport and chemical properties. Several improvements (outlined in Chapter 4) will be required in order for the window to survive temperatures used in the crystallization zone of ammonothermal growth (~600 ºC). Raman detection of dissolution of Ga feedstock and amide mineralizer will hopefully permit identification of the soluble intermediate(s).

The decomposition of sodium azide has been observed by Raman spectroscopy at supercritical conditions. Sodium amide is formed as a result of this reaction. Additionally a large overpressure of N_2 (and presumably H_2) is created during breakdown. This overpressure could be favorable by altering the transport properties or by inhibiting ammonia breakdown by the Haber process. The rate and temperature of decomposition have been qualitatively verified by Raman spectroscopy. Future work with this technique may help optimization of ammonothermal GaN growth conditions such as temperature, gradient, choice of mineralizer, and fill percent.

References

1) S. Nakamura, S. Pearton, and G. Fasol, *The Blue Laser Diode: The Complete Story* (Springer-Verlag, Berlin, 1997).

2) M. A. Khan et al., Applied Physics Letters, 62, 1786 (1993).

3) L. Liu and J. H. Edgar, Materials Science & Engineering R-Reports, 37, 61 (2002).

4) S. Pendurti, Q. S. Chen, and V. Prasad, Journal of Crystal Growth, 296, 150 (2006).

5) A. Yoshikawa, E. Ohshima, et al., Journal of Crystal Growth, 260, 67 (2004).

6) P. G. Jessop and Walter Leitner, *Chemical Synthesis Using Supercritical Fluids* (Wiley-VCH, New York, 1999).

7) D.R. Ketchum and J.W. Kolis, Journal of Crystal Growth, **222**, 431 (2001).

8) B. Wang, M.J. Callahan, J. W. Kolis et al., Journal of Crystal Growth, 287, 376 (2006).

9) B. Wang and M.J. Callahan, Crystal Growth and Design, **6**, 1227 (2006).

10) J. W. Lundeen and W. H. Koehler, The Journal of Physical Chemistry, 79, 2957 (1975).

11) M. Schwartz and C. H. Wang, The Journal of Chemical Physics, 59, 5258 (1973).

12) Y. Ikushima, K. Hatakeda, N. Saito, M, Arai, Journal of Chemical Physics, **108**, 5885 (1998).

13) D.M. Carey and G. M. Korenowski, Journal of Chemical Physics, **108**, 2669 (1998).

14) H.E. Stanley, *Introduction to Phase Transitions and Critical Phenomena*, (Clarendon Press, Oxford, 1971).

15) W.H. Koehler et al., The Journal of Physical Chemistry, **83**, 3264 (1979).

16) T. Ujike and Y. Tominaga, Journal of Raman Spectroscopy, **23**, 485 (2002).

17) M. Buback and K.R. Schulz, The Journal of Physical Chemistry, **80**, 2478 (1976).

18) J. Mellqvist and A. Rosen, J. Quant. Spectsoc. Radiat. Transfer, **56**, 187 (1996).

19) J. F. Bertran and B. La Serna, Journal of Molecular Structure, **56**, 283 (1979).

20) P. Gans and J. B. Gill, Faraday Discussion, 64, 150 (1977).

21) P. J. Smits, I. G. Economou, et. Al, Journal of Physical Chemistry, 98, 12080 (1994).

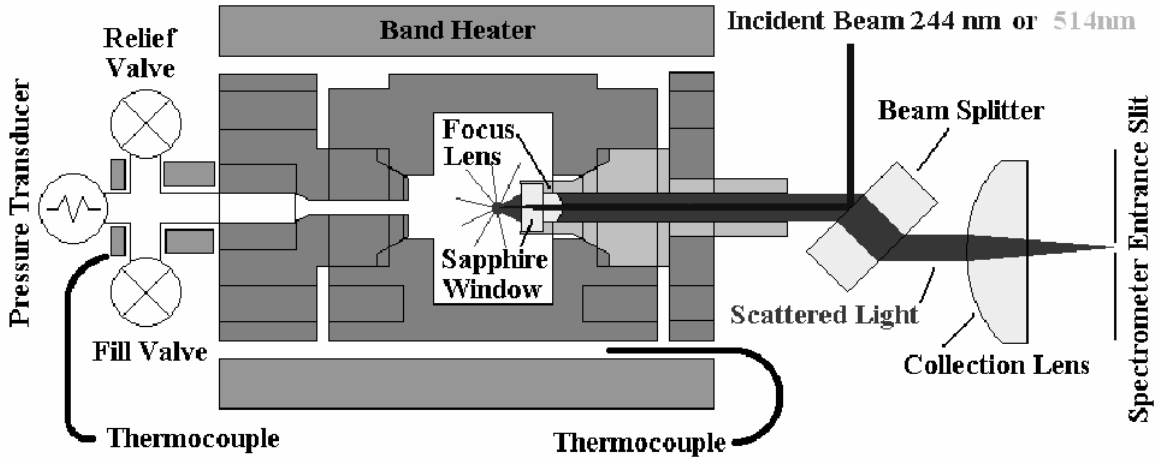

Figure 2.1 Schematic of the high temperature, high pressure autoclave.

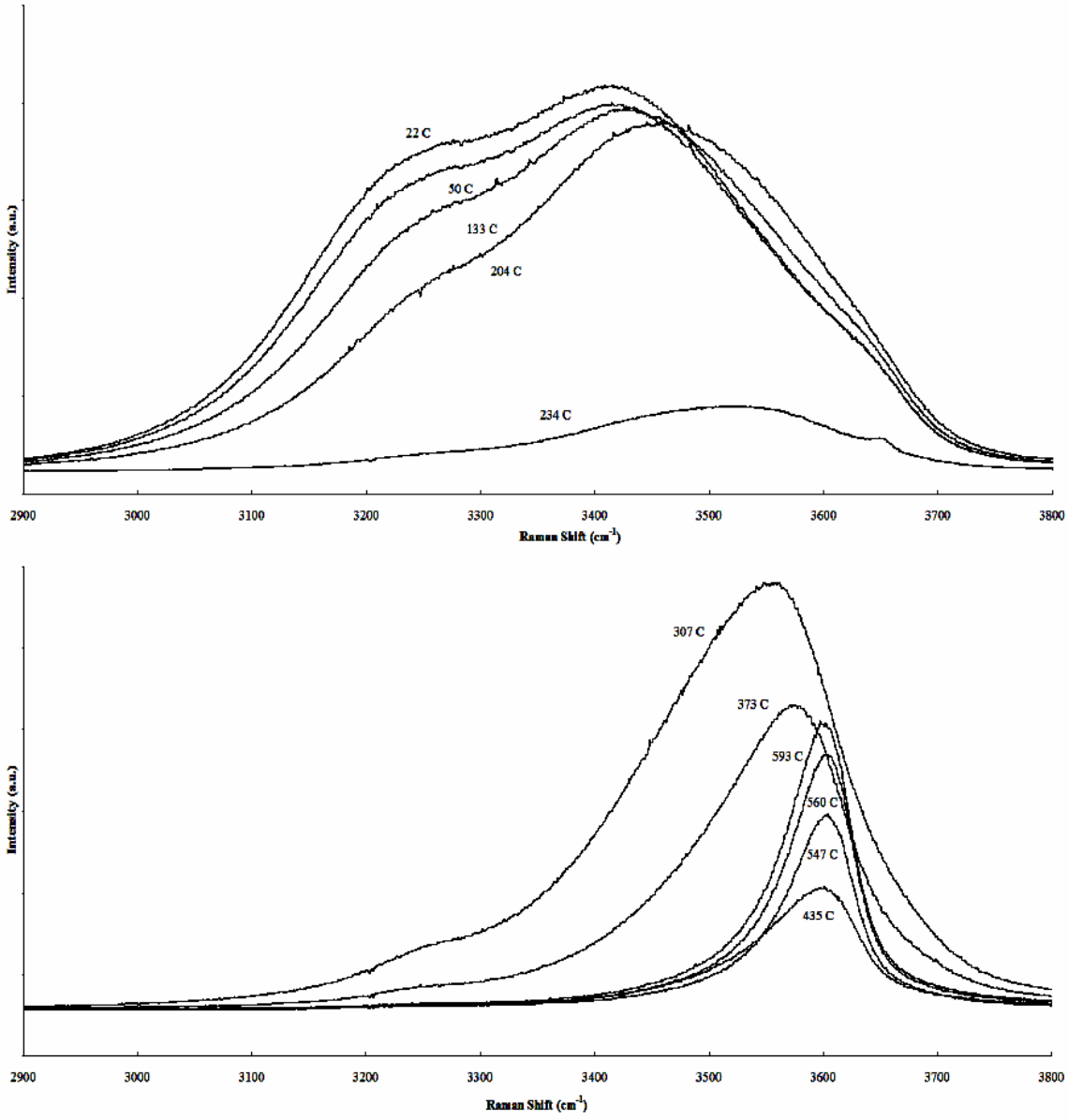

Figure 2.2 UV Raman scattering from supercritical water.

The intensity scale of the lower graph has been increased to show less intense peaks.

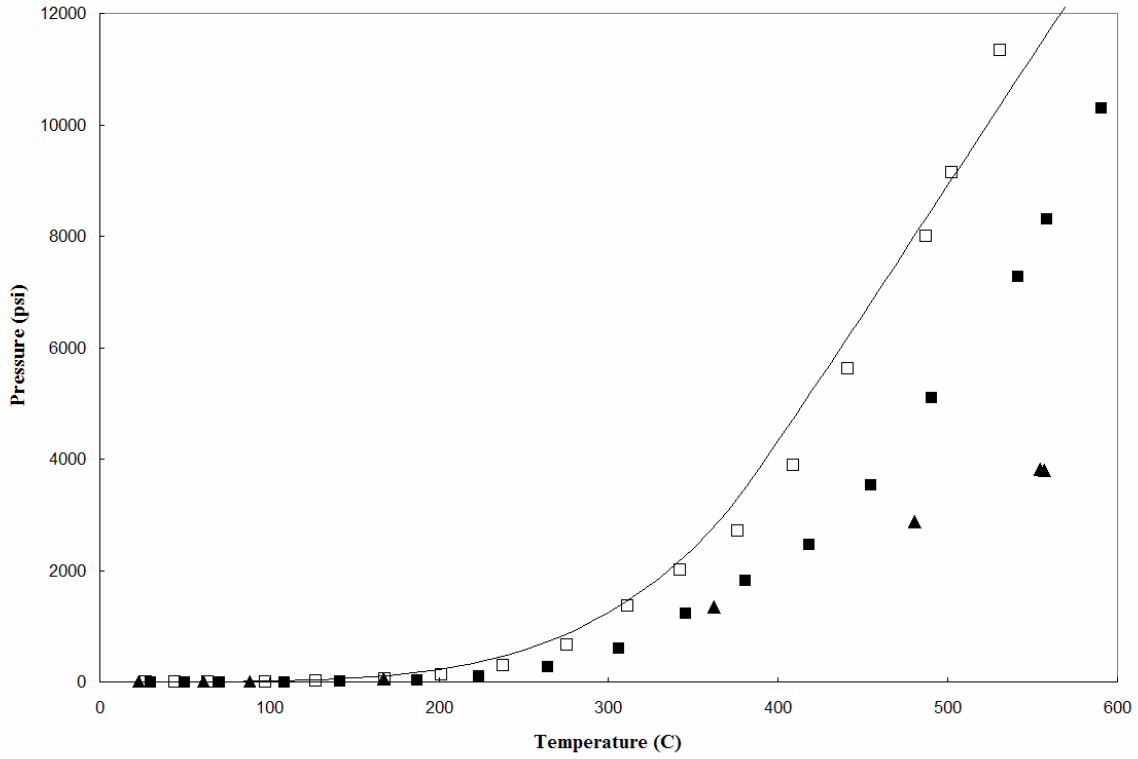

Figure 2.3 Temperature-pressure relationship for supercritical water.

Recorded pressure data for two water fills at 50% (■) and 25% (▲) are shown along with the theoretical P-T data from Reference 21 (solid line). Corrected data (□) are adjusted for temperature errors caused by thermocouple placement and non-linear pressure shifts due to heating of the pressure strain gauge.

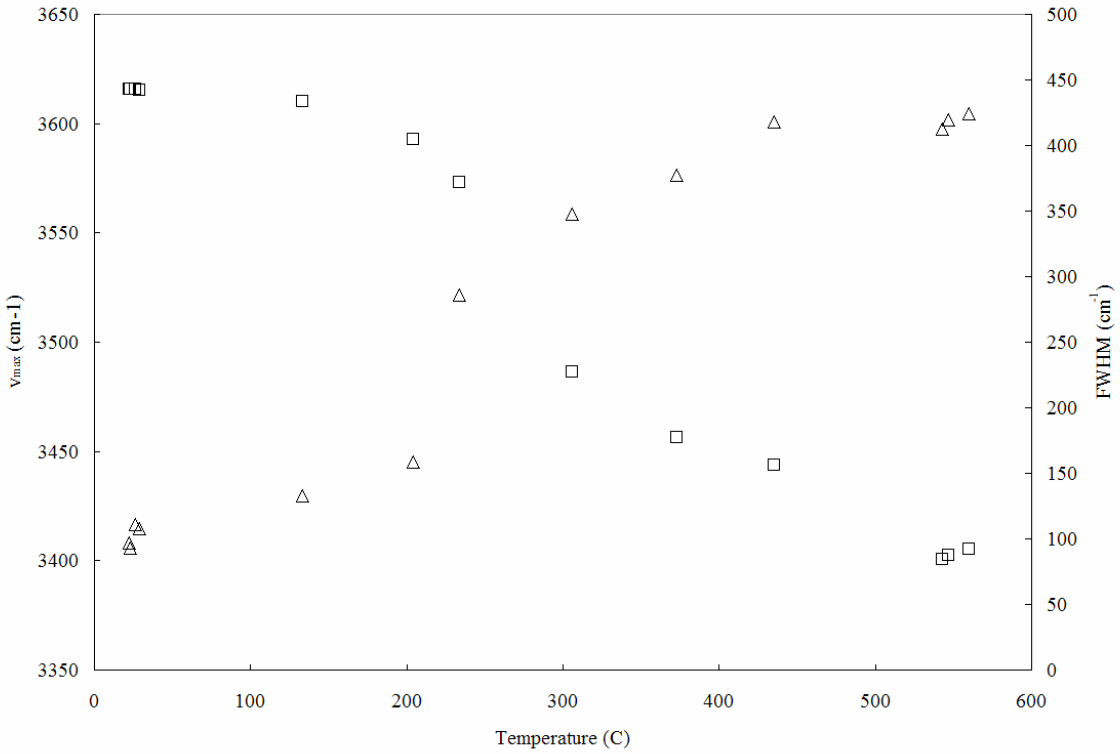

Figure 2.4 ν_{max} and FWHM of the O-H stretch of supercrtical water.

ν_{max} (Δ) and FWHM ($\square$) of the O-H stretch region of water for a 50% fill are presented.

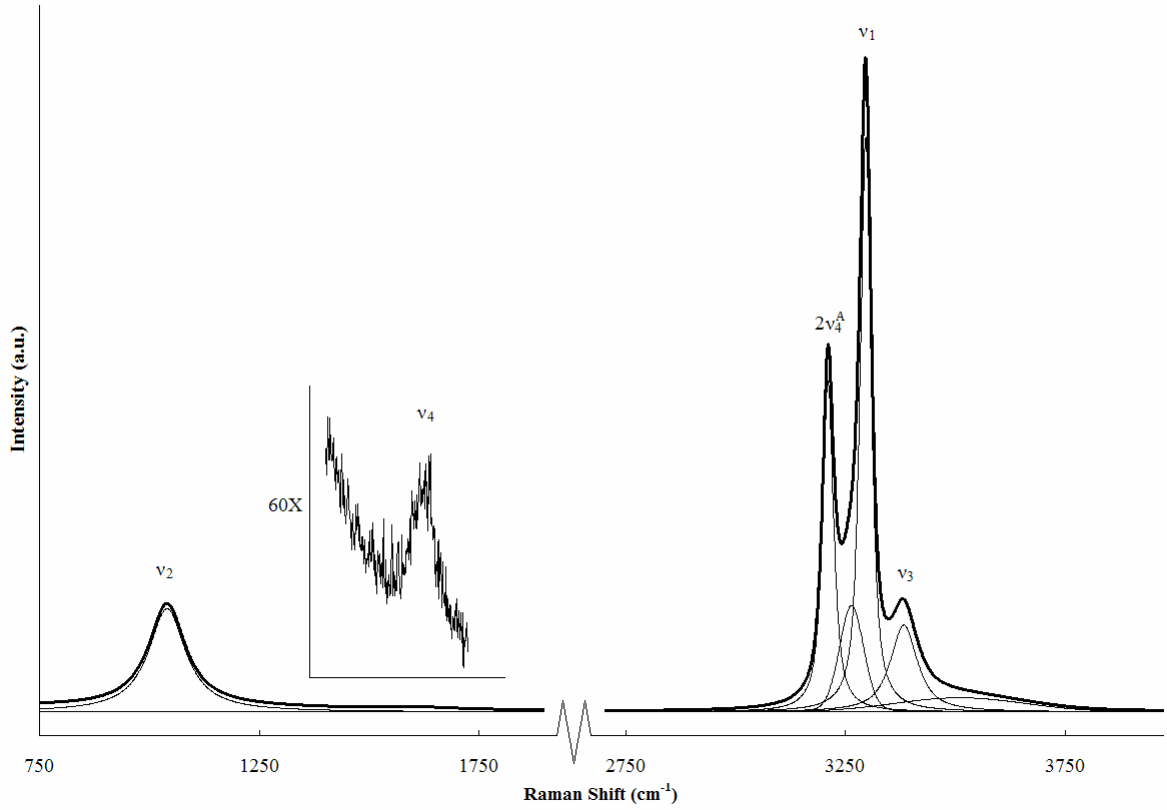

Figure 2.5 UV Raman of liquid ammonia at 20 ºC and 135 psi.

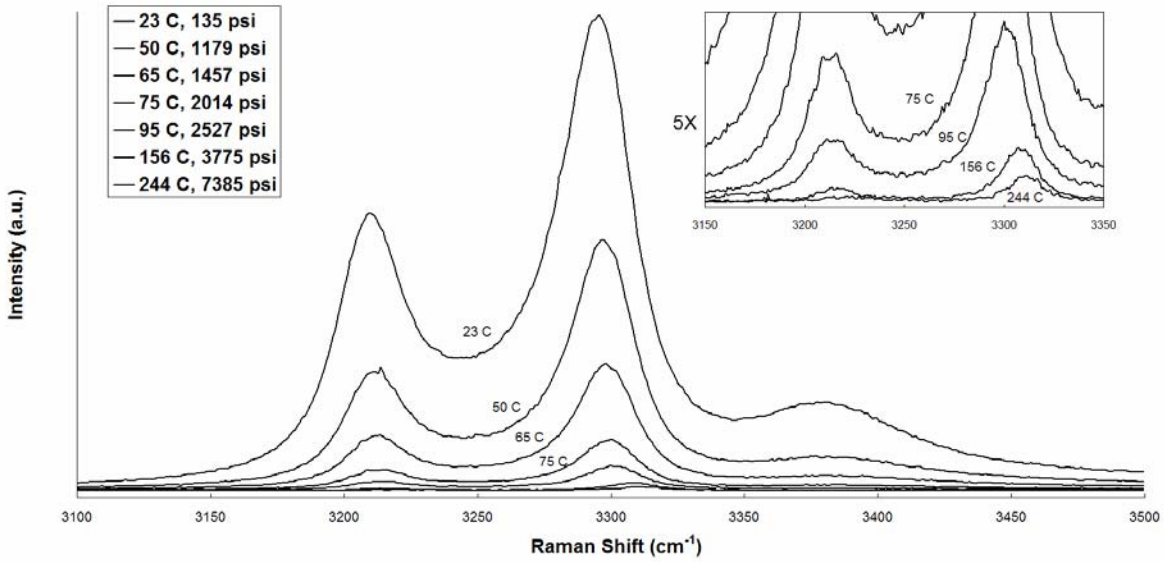

Figure 2.6 UV Raman of ammonia between 23 and 244 ºC and 135 to 7300 psi.

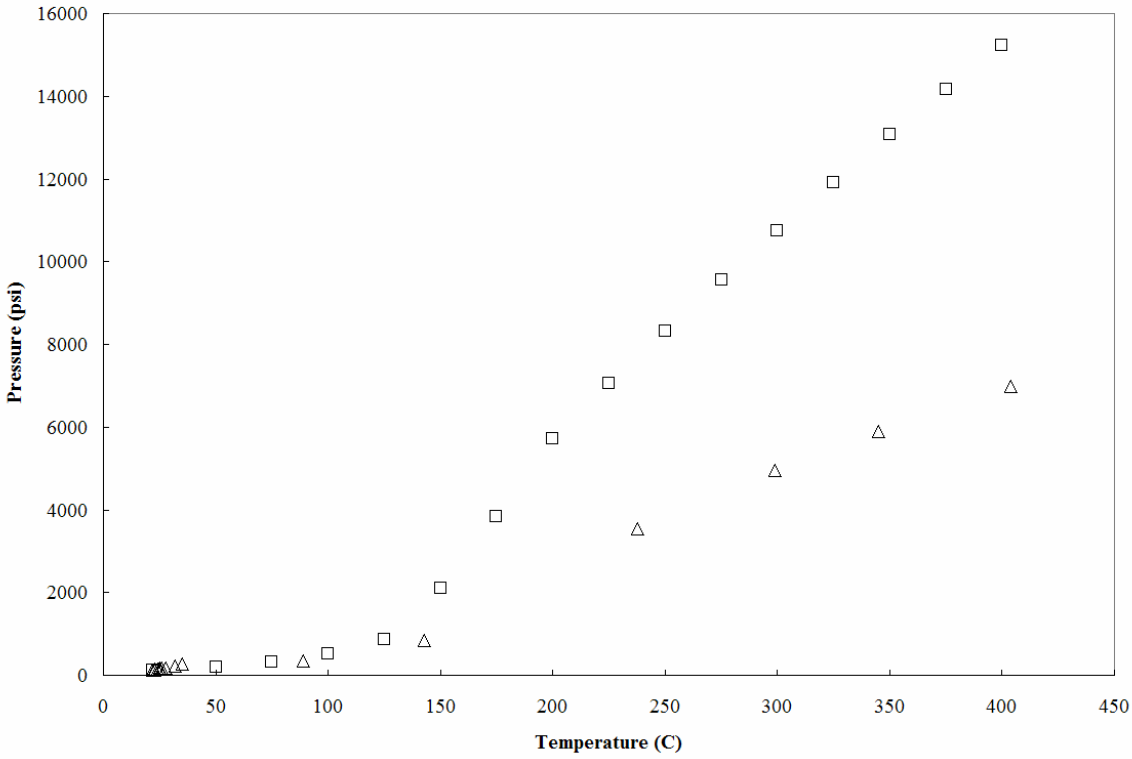

Figure 2.7 Temperature-pressure relationship for supercritical ammonia. Pressure data for two fills at 40% (Δ) and 50% (□) are plotted as a function of temperature.

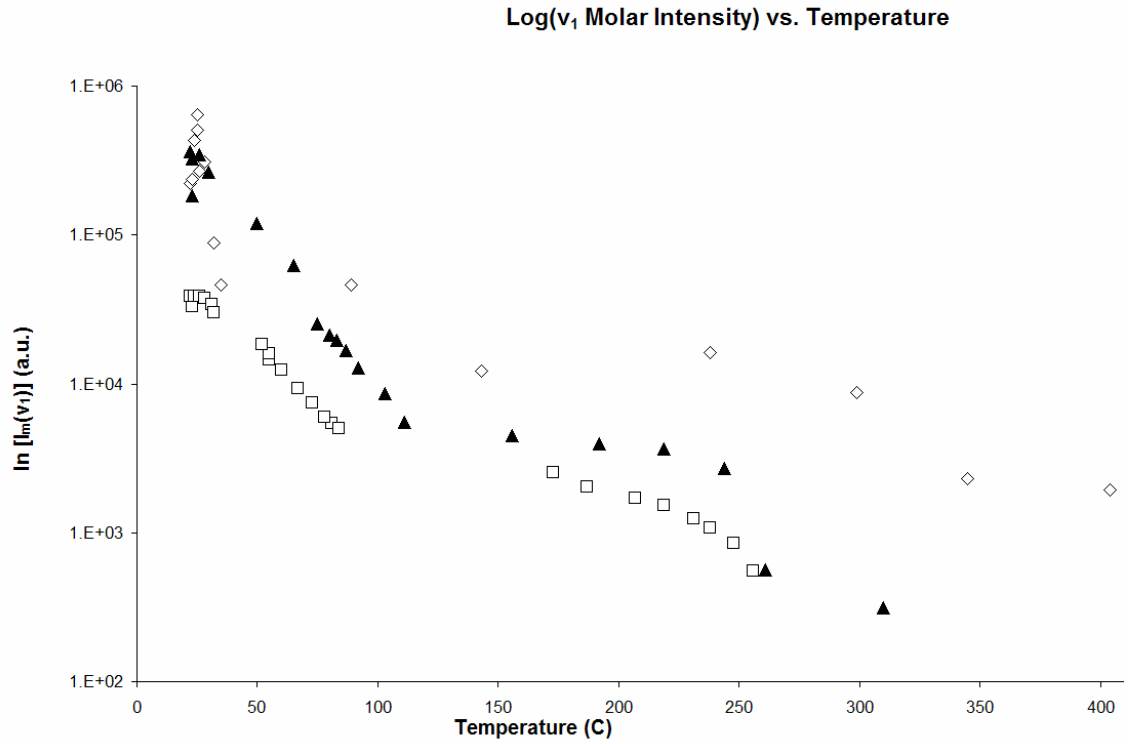

Figure 2.8 Log ammonia ν_1 molar intensity vs. temperature

Intensities of the ammonia ν_1 mode is shown to decrease exponentially with temperature for three fill percents: 40% (▲), 50% (○) and 65% (□).

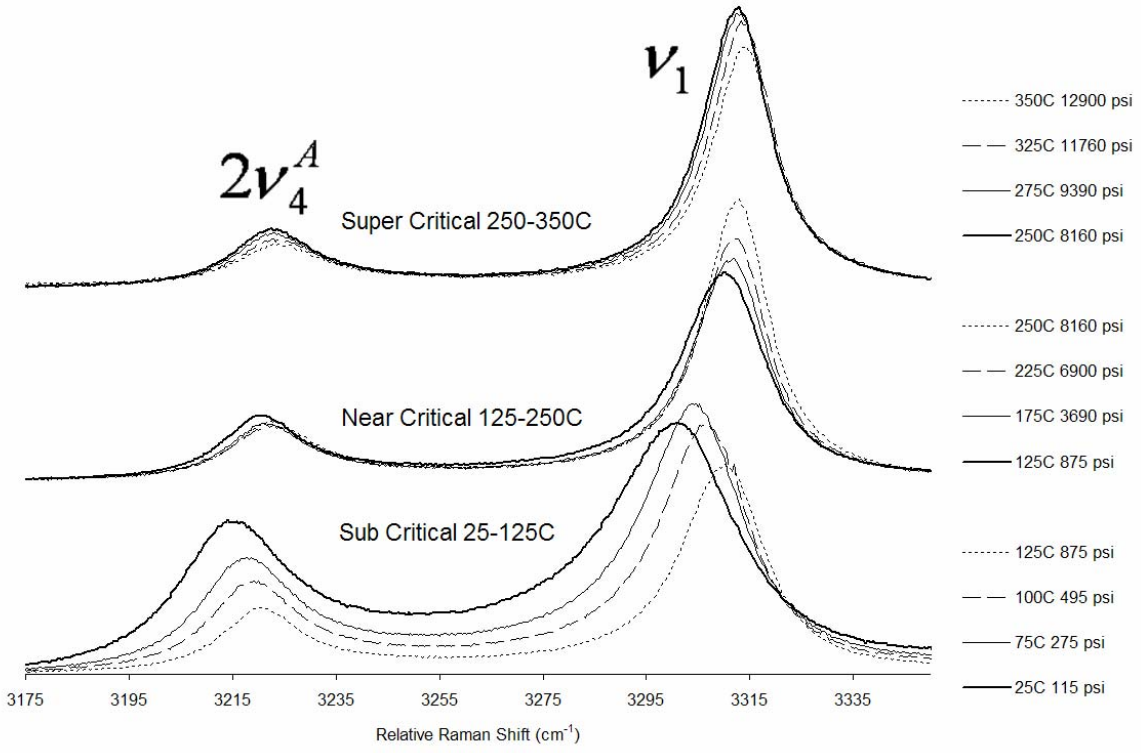

Figure 2.9 Visible Raman of supercritical ammonia to 350 ºC and 13 kpsi.

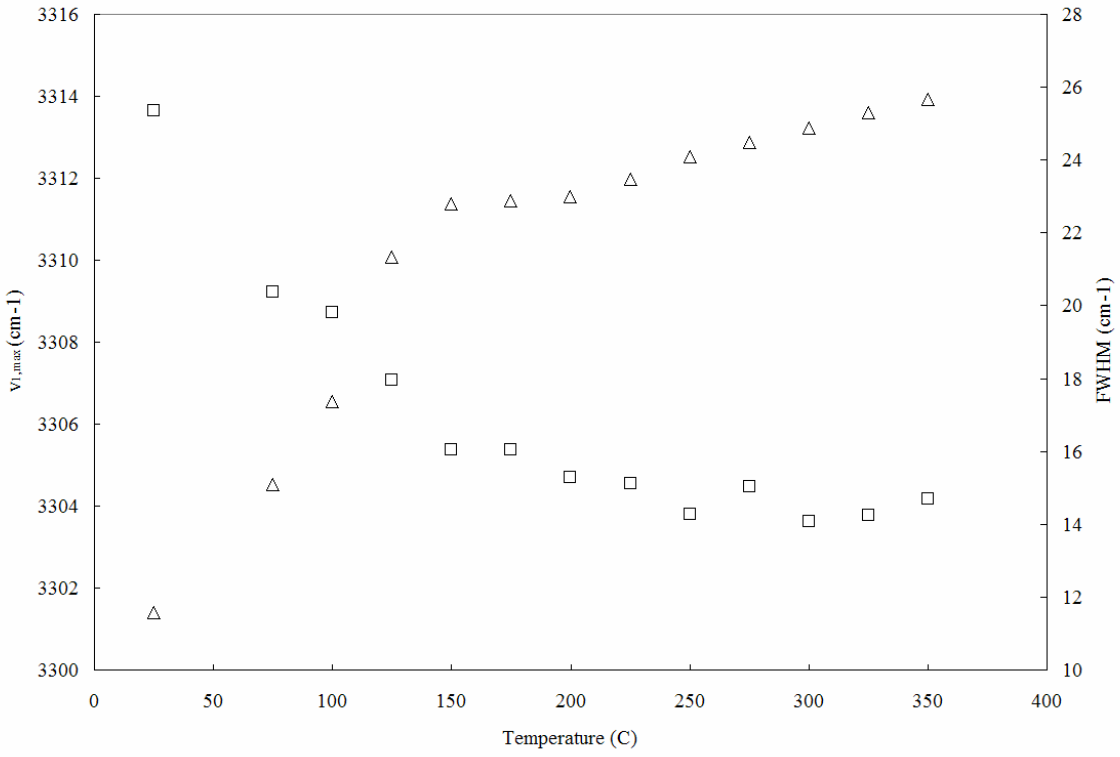

Figure 2.10 $\nu_{1,max}$ and FWHM of the N-H stretch of supercrtical ammonia. $\nu_{1,max}$ (Δ) and FWHM (□) of the ammonia N-H symmetric stretch for a 65% fill are presented.

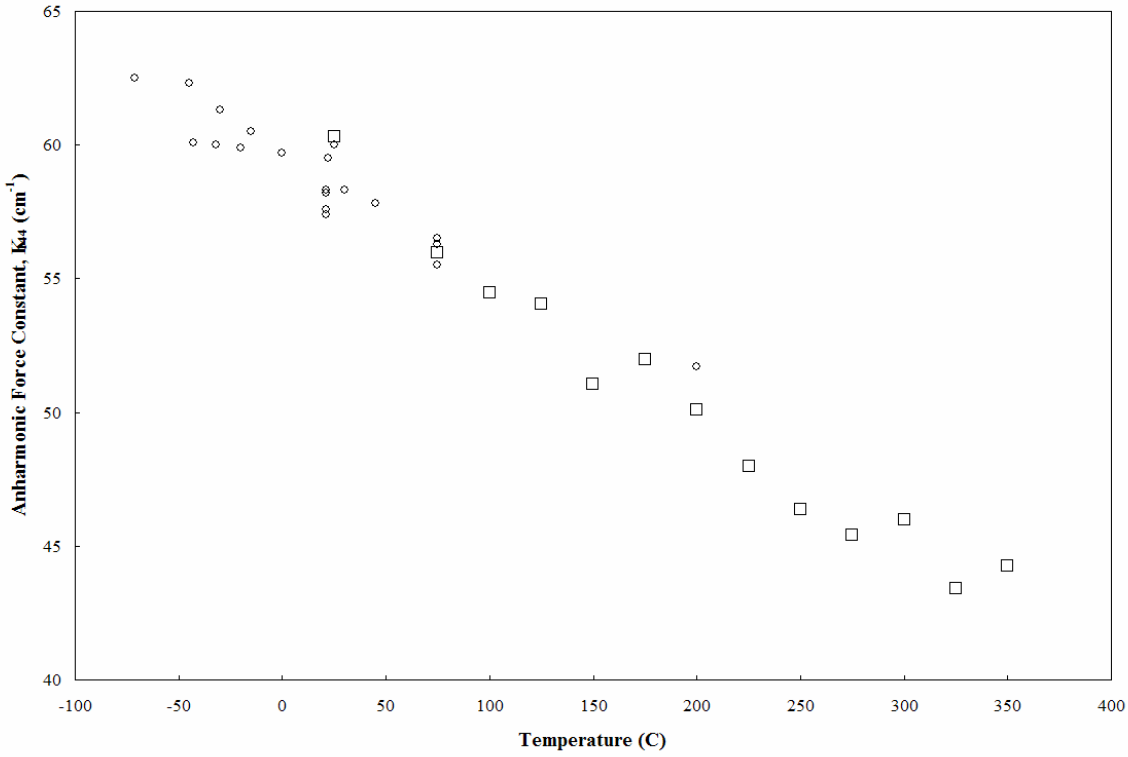

Figure 2.11 Temperature dependence of anharmonic force constant, K_{144}. Anharmonic force constants, K_{144}, for a 65% ammonia fill (□) are plotted as a function of temperature and are compared to data from Reference 19 (º).

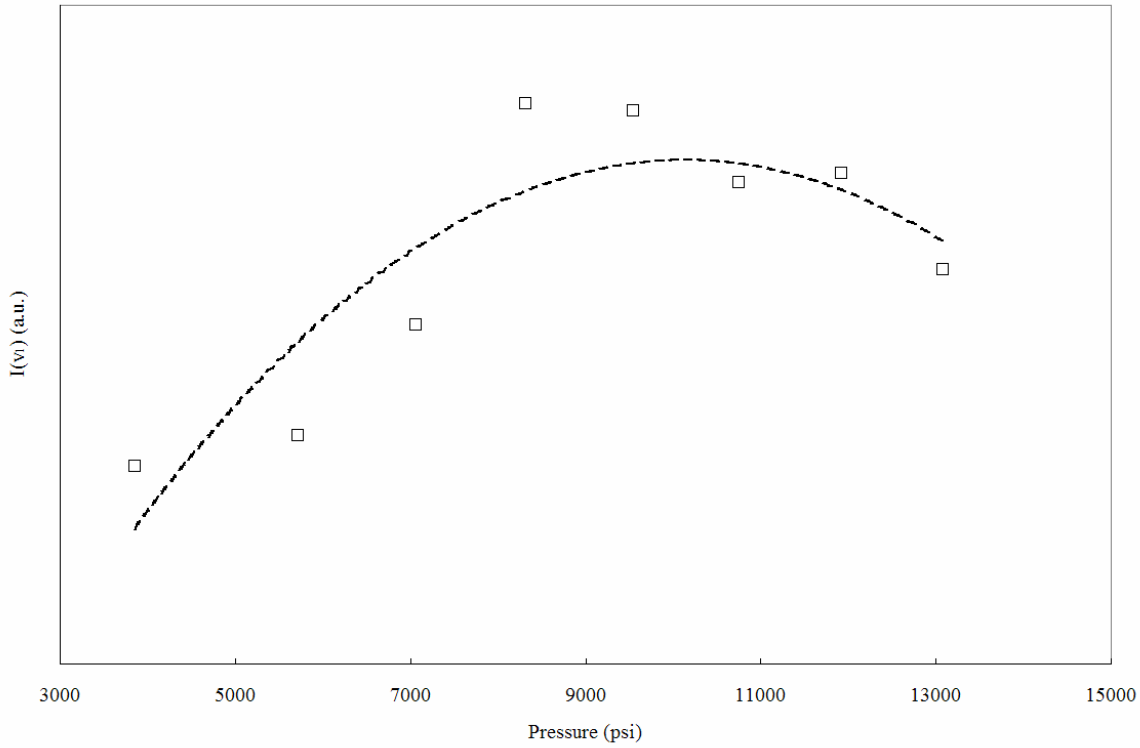

Figure 2.12 Intensity of NH_3 ν_1 band as a function of pressure.

Intensity of the NH_3 ν_1 band (□) for a 65% fill is plotted as a function of pressure. The dashed line is a 2^{nd} degree polynomial fit whose maximum occurs at 10 kpsi.

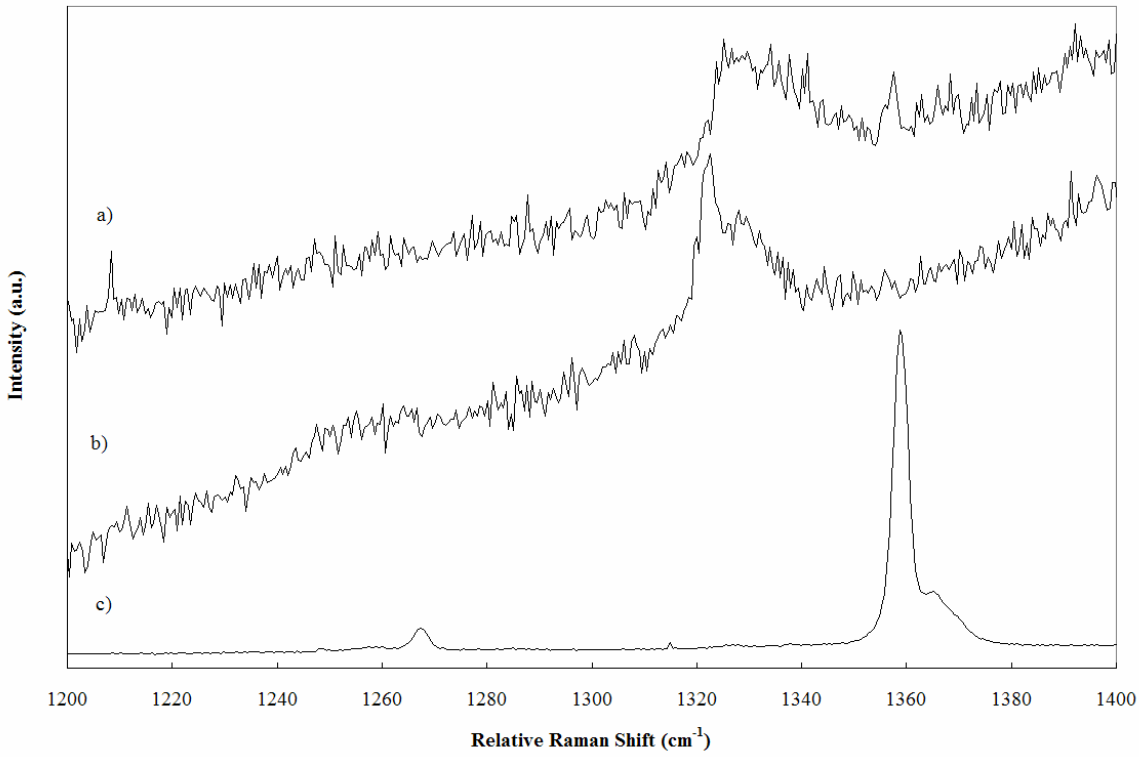

Figure 2.13 Raman spectra of solid and solvated NaN_3.

Raman spectra of NaN_3 solid (c) is compared to the solvated spectrum at 25 (b) and 275 ºC (a).

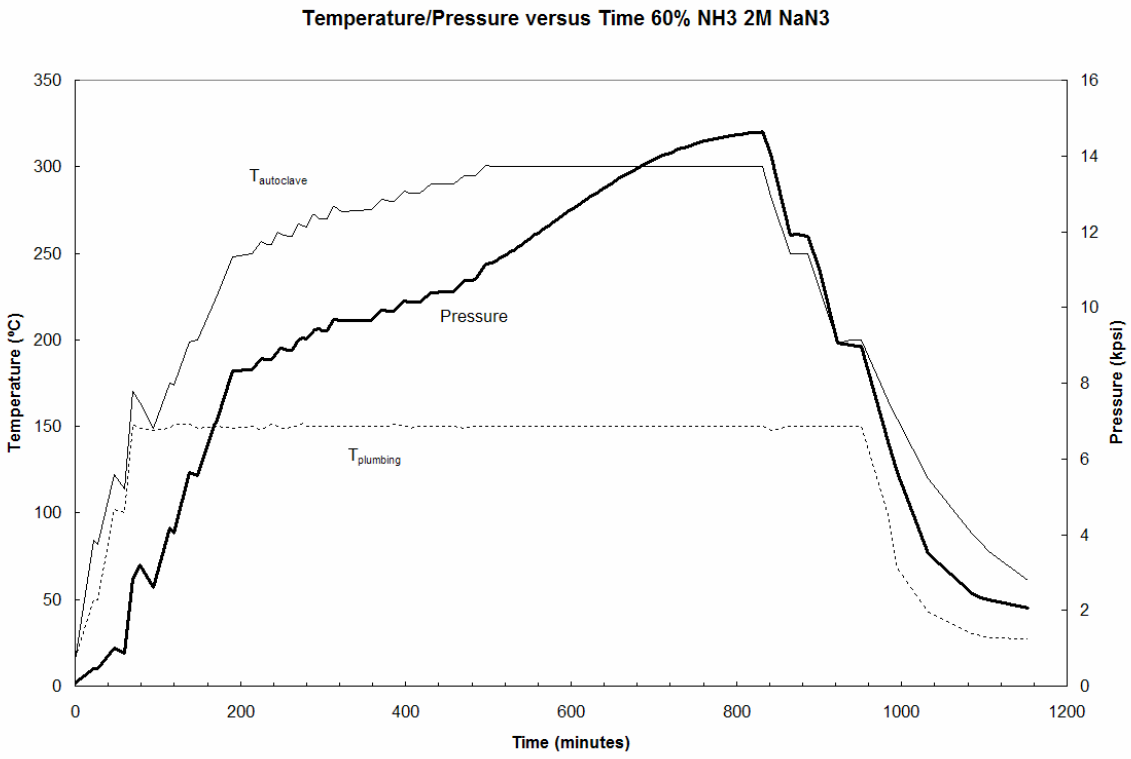

Figure 2.14 Temperature and pressure changes in time during azide decomposition. Pressure (dark line), autoclave temperature (light line), and plumbing temperature (dashed line) are plotted as a function of time.

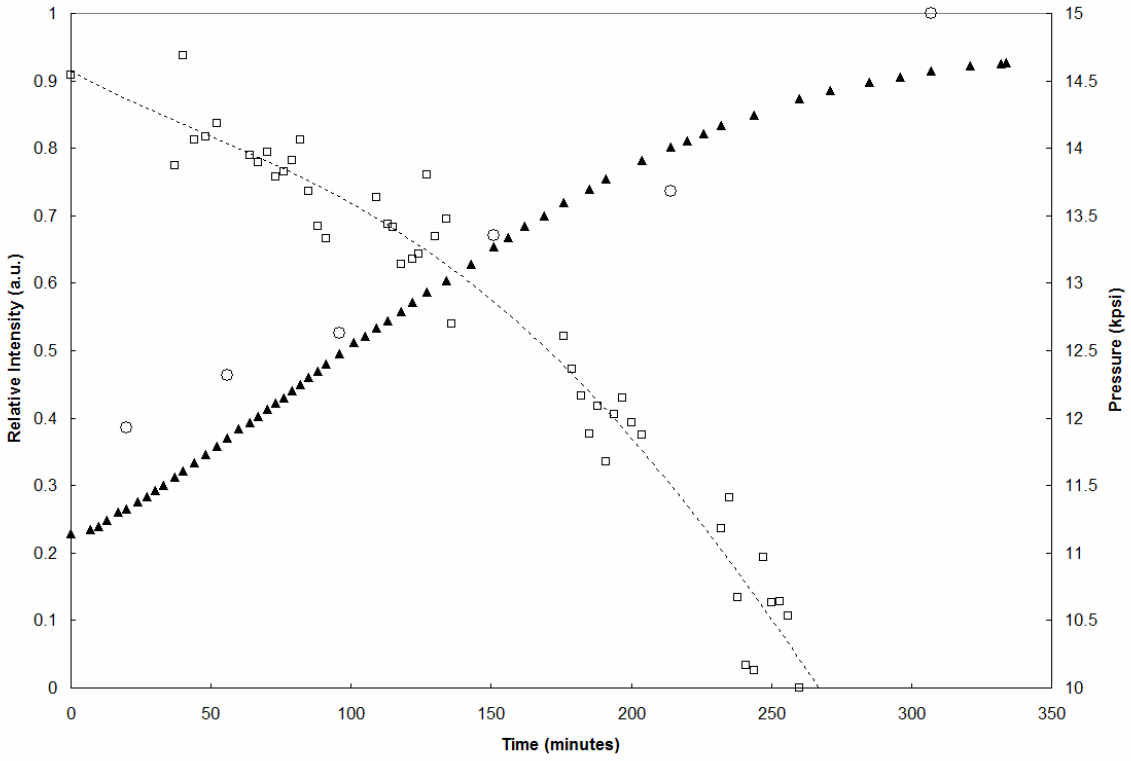

Figure 2.15 Azide and nitrogen Raman intensity and pressure vs. time.

N_2 ν_1 (○) and N_3^- ν_3 (□) Raman intensities and pressure (▲) are plotted for a 65% NH_3 fill with 2.0 M NaN_3. Throughout these measurements the temperature was maintained at 300 C. The dashed line is a guide for the eye showing that the rate of azide decomposition apparently increased over these times.

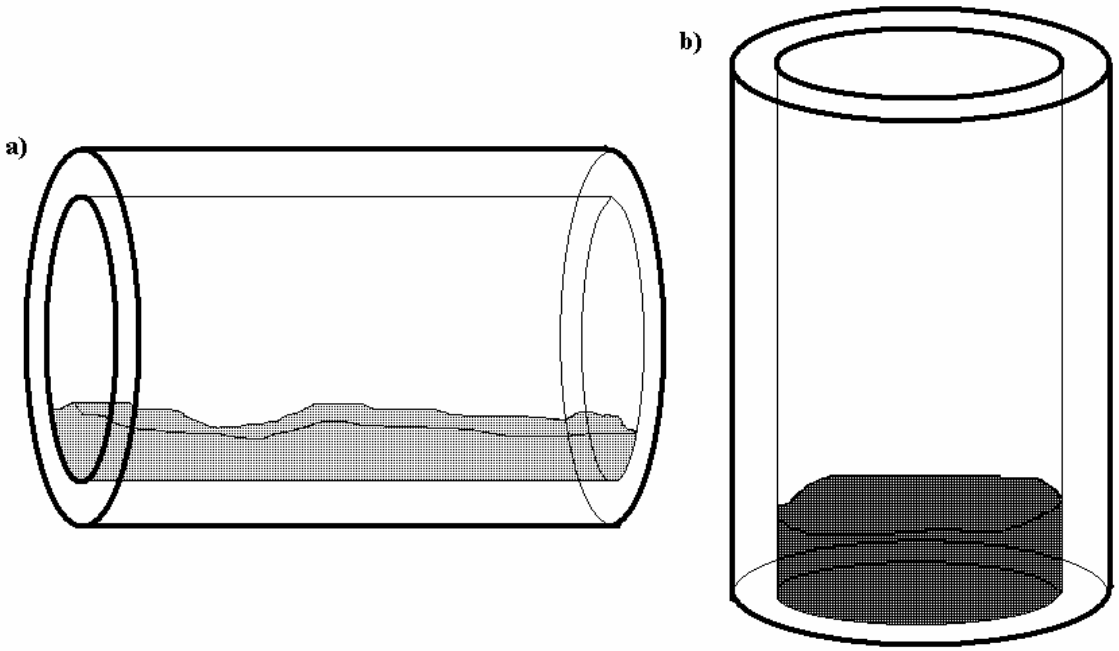

Figure 2.16 Schematic of location of precipitates after autoclave evacuation. The autoclave is filled and evacuated in the orientation shown in (b). For fills that did not exceed 275 ºC the sodium azide was recovered and found in the position shown in (b) signifying that the azide came out of solution during ammonia evacuation. Spectroscopy and heating are performed while the cell is oriented as shown in (a). For fills that exceeded 275 ºC sodium amide was found in the location displayed in (a) meaning that it came out of solution at temperature or during cooling.

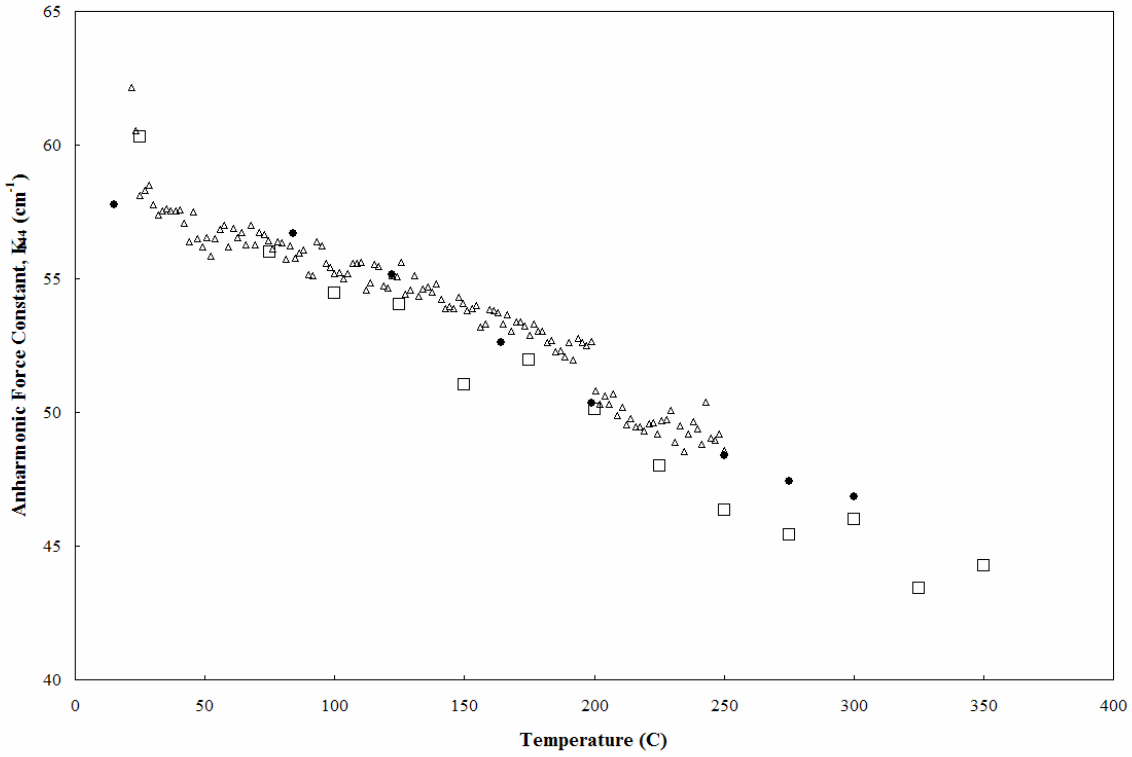

Figure 2.17 Temperature dependence of K_{144} in azide-ammonia system.

Anharmonic force constants, K_{144}, are plotted as a function of temperature for a 65% ammonia fill (□) and for a 60% ammonia fill with 0.5 M NaN_3 (∆) and a 65% ammonia fill with 2.0 M NaN3 (●).

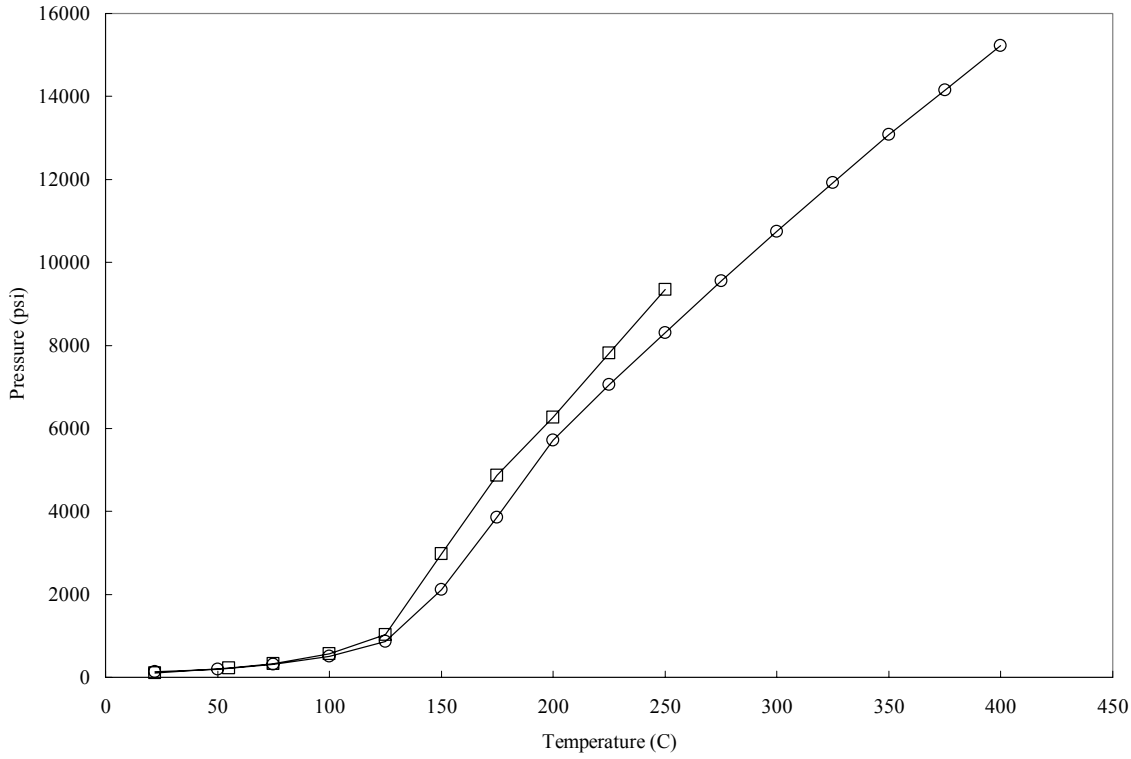

Figure 2.18 Temperature-pressure relationship for azide-ammonia system. Pressure data for 65% neat ammonia (□) and 65% ammonia with 2.0 M NaN_3 (○) fills are plotted as functions of temperature.

3. Surface Enhanced Raman Spectroscopy of Silver Nanostructures Grown by Ferroelectric Lithography

ABSTRACT

Silver nanowires created by photoreduction of silver nitrate on periodically poled lithium niobate substrates are evaluated for use in Surface Enhanced Raman Spectroscopy (SERS). SERS increases scattering intensities by factors of 10^6 or more enabling submonolayer or even single molecule detection. The technique relies on a suitably roughened silver surface to excite surface plasmon resonance. Many current SERS substrates suffer from lack of reproducibility, and ferroelectric lithographic control over silver nanoparticle position, shape, and size could help overcome this deficiency. With this technique, silver selectively deposits on domain boundaries forming nanowires with roughness features on the order of 10-100 nm which is appropriate for SERS with visible excitation. In this study, pyridine, benzoic acid, and Rhodamine 6g are used as analytes. Spatially periodic enhancement factors are observed as the laser spot is moved perpendicular to the wires; however, the periodicity has the frequency of the domains not that of the wires. Laser induced photographitization occurs on positive domains and forms a SERS active carbon layer which obscures the enhancement from the wires. Scanning Auger Microscopy (SAM) shows that a small amount of silver normally undetected by Atomic Force Microscopy (AFM) is on the positive domains.

3.1 Introduction

Surface enhanced Raman spectroscopy (SERS) has had a revival in popularity recently due to its possible use in biodetection and single molecule spectroscopy SERS. [1] The increased enhancement factor due to interparticle interaction allows detection of submonolayer or single molecule detection.[2] In order to avoid reliance on hot spots, control over nanoparticle shape, size, and location must be achieved. Ferroelectric lithography offers this control and nanowires created by this technique are evaluated in this study as SERS substrates.

Early on in the development of the SERS mechanism, Creighton et al. observed that the maximum enhancement factors were attained at the wavelength that corresponded to the maximum of the extinction spectrum.[3] The extinction spectrum is the addition of the scattered and absorbed and is given by Mie theory.[4] Below the Rayleigh limit ($R = \lambda / 20$) the extinction spectrum is not a strong function of particle size, but above this limit, the extinction maximum increases with particle size. In order to achieve highest enhancement factors, the surface plasmon resonance must be optimally excited which requires coordination of the size of the particle and excitation wavelength. For visible excitation this corresponds to silver nanospheres with radius 30 to 90 nm.[3] The shape of the nanoparticles also affects the optimal excitation wavelength and can add to the enhancement factor by the so called "lightning rod effect." [5]

Substrate materials have ranged from the alkali metals[6] to Al[7] to In[8], but the coinage metals, Ag, Au, and Cu, display the greatest enhancement factors.[9] Silver, in particular, is most suited for surface plasmon resonance owing to its low plasma

frequency.[10] The low plasma frequency and small imaginary component of the dielectric constant create a sharp, intense resonance ideal for SERS. Also, the position of the extinction band maximum will be a function of the real component of the dielectric function of the substrate material. It was shown in Chapter 1 that for nanospheres, plasmon resonance occurs when

$$\mathrm{Re}\,\varepsilon(\omega_R) = -2\varepsilon_0 .$$

This condition is met for silver in the visible range.[3]

Capacitive field effects of nanoparticle arrays can further increase enhancement factors by five orders of magnitude.[11] When the interparticle spacing is on the same order of magnitude as the particle diameter, interparticle interactions can strongly affect the optical response, especially when the incident electric field is polarized in the direction of the interparticle seperation.[1] Zhao et al.[12] showed that the resonance was optimally tuned for interparticle separation, D, and particle radius, R when

$$D/(2R)=5.$$

Silver nanowires created in this study by ferroelectric lithography exhibit roughness features and particle sizes[13] that are appropriate to surface enhancement with visible excitation.

3.2 Experimental

Periodically poled lithium niobate (PPLN) substrates measuring 0.5 mm square were purchased from Crystal Technologies. The samples were cleaned by ultrasonication in acetone and methanol each for 20 minutes. PPLN samples were reused after silver deposition and SERS analysis. AFM and XPS confirmed all silver was removed by sonication.

Silver was deposited on the samples by photoreduction of silver nitrate. One drop of 0.01 M aqueous sodium nitrate was placed on the cleaned sample. The sample was illuminated by an Oriel Instruments Hg lamp. The primary line of the the Hg emission spectrum is at 254 nm which is above the band gap of lithium niobate. Illumination times ranged from 30 seconds to 15 minutes, however reported results are from 3 minute illumination times unless otherwise noted. After deposition, samples were rinsed in deionized water and blown dry with forced nitrogen. Atomic force and piezoresponse force microscopy (AFM and PFM respectively) data were recorded by a Park Scientific Instruments Model Autoprobe M5.

For SERS analysis, samples were mounted on a specially prepared microscope slide shown in Figure 3.1. A small drop of analyte in solution was added to the sample and was covered by a glass cover slip. Samples normally remained wet throughout SERS detection. The sample and slide were mounted on an XY micrometer stage with 2 μm resolution. Micro-Raman data were obtained using a BH3 Olympus microscope attached to a Spex U1000 double monochrometer. The 479, 488, and 514 nm lines of a Coherent I-

90 argon ion laser were used as excitation. The laser was focused to a Gaussian spot of approximately 3 μm in diameter.

Scanning Electron Microscopy (SEM) images were taken on a JEOL 6400F Field Emission SEM with Everhart-Thornley (E-T) secondary electron detector. Scanning Auger Microscopy was performed at the University of Florida's Major Analytical Instruments Center on a Physical Electronics NE5660 Scanning Auger Multiprobe.

3.3 Results and Discussion

3.3.1 Spatial Periodic Surface Enhancement from Silver on PPLN

Prior research has established that silver preferentially deposits on domain boundaries under ordinary deposition conditions as can be seen in Figure 3.2. [13] Because $LiNbO_3$ has a relatively low defect density, the internal polarization is screened primarily by surface charges.[13] This external screening leads to singularities in the electric field near the surface.[14] The electric field has a maximum at the domain boundaries. Electrons excited into the conduction band by the UV illumination are attracted to the domain boundaries by this field where they reduce silver ions in the $AgNO_3$ solution. The wires produced by this technique are actually chains of roughly hemispherical clusters ranging from 30 to 150 nm in diameter as can be seen in the inset of Figure 3.2.

Initial SERS studies utilized pyridine in aqueous solutions ranging from 10^{-4} to 10^{-1} M. Substrates with silver and analyte in these concentration ranges showed signifigant enhancement of the pyridine signal. Substrates without silver showed no enhancement and the pyridine was undetectable. The spectra of two samples, one with and one without silver, each with 0.01 M aqueous pyridine are shown in Figure 3.4. All bands below 900 cm^{-1} that are shared by both spectra are typical of $LiNbO_3$.[15] The two bands at 1006 and 1023 cm^{-1} are the ring breathing modes of pyridine that are shifted slightly to larger Raman shifts, typical of pyridine adsorbed on silver.[16] The broad features at 1350 and 1500 cm^{-1} are associated with amorphous carbon.[17] Inclusion of these carbon bands is typical in SERS experiments and will be discussed further in the next section.

When the laser is scanned across the sample in a direction perpendicular to the wires, the enhancement of the pyridine breathing mode varied periodically. When scanning parallel to the wires, the enhancement was nearly constant. These trends are shown in Figure 3.5. The maxima in this figure are 20-28 microns apart. Wire separation is expected to be half of this. Also, the half-widths of the peaks are up to 10-18 microns wide. The assumption is that the enhancement is not from the wires alone.

The periodicity of the enhancement factor was invariant to deposition time between 30 seconds and 15 minutes. Although, at longer deposition times (greater than 10 minutes), enhancement is present at all positions (i.e. the minima do not go to zero), but the trend is still periodic with the same frequency.

The period of enhancement was also invariant to analyte type (including benzoic acid and Rhodamine 6g), analyte concentration, and excitation frequency (479, 488, and 514 nm). Pyridine excited with 514 nm light showed the most intense signal (although, not necessarily the most enhancement) and was used for most measurements. Rhodamine fluorescence (which will also be enhanced by surface resonance) was extremely intense and the Raman signal could only be detected with 479 nm excitation.

Pyridine was detected at 10^{-6} M but not at 10^{-8} M. Benzoic acid and Rhodamine 6g were studied at concentrations between 10^{-2} and 10^{-4} M, but no attempts were made to determine a low detection limit.

3.3.2 Laser Damage

Optical micrograph images of samples obtained after SERS characterization showed significant damage in the regions where the laser light was incident on the surface. The damage regions appeared as bright, reflective areas in the optical microscope images that are normally only present on one of the two domains. By defocusing the laser spot a uniform laser damage region can be created with an approximately 30 μm diameter. After the analyte solution had dried, AFM and PFM were performed to determine that the laser damage occurred exclusively on the positive domains (Figure 3.6). The AFM topography results show that the damage is actually deposition of a surface layer as thick as 0.2 μm. On PPLN samples without silver nanowires, no laser damage occurred. The damage phenomenon was also dependent on the presence of an analyte.

Laser induced damage observed on silver electrodes in electrochemical SERS studies have been explained as surface enhanced photodissociation of either the adsorbed analyte or dissolved CO_2 resulting in a disordered carbon layer. [18] The electromagnetic enhancement mechanism responsible for SERS also affects other phenomenon associated with the interaction of a molecule and an electromagnetic field such as luminescence, absorption, and photochemistry. [19]

It was also found that these damaged regions were still Raman active even when the analyte had dried. (Normally, enhancement is only seen on samples which are still wet.)

Because the laser damage required silver, it is hypothesized that the damage occurs exclusively on the positive domains because residual amounts of silver are deposited in

that region during illumination. AFM of longer depositions showed that silver eventually begins to decorate the entire positive domain (Figure 3.3). This is explained by noting that, while the electric field created by polarization and screening charges has a maximum at the domain boundary, the field near the positive domain will still be positive and therefore attractive to conduction band electrons. [14]

Although silver islands located away from the wire are occasionally detected, they are not consistently observed to be preferentially located on either domain. In depositions with illumination time less than or equal to three minutes, on-domain silver was not normally detected by AFM. SEM was also not able to detect interstitial silver. SEM images of a 3 minute deposition showed that most of the silver was on the wires (Figure 3.7). There were some small islands (also observed occasionally in AFM) on the domains, but they were not preferential to either domain.

SAM was performed on a sample with silver deposition time equal to 5 minutes. An Auger scan taken from a positive domain is shown in Figure 3.8, and an Auger line scan taken in a direction perpendicular to the domain stripes is shown if Figure 3.9. The theoretical spatial resolution of the SAM electron source is 0.5 μm. The SAM line scan shows results similar to that of the SERS characterization; the period and width of peaks are in accordance with those of the domains. This finding is consistent with the theory that residual silver is located on the positive domain. The fact that SAM line scans did not detect the wires is attributed to lack of spatial resolution. Because LiNbO3 is insulating, a high scattering angle had to be used (60º) which will adversely affect the spatial resolution.

By decreasing the incident laser power to <1mW, laser damage did not occur even after up to 1 hour of exposure. Unfortunately, at these laser powers, analyte Raman signal

was not detected from the undamaged regions. These laser powers could be used, however, to collect SERS scattering from regions previously damaged by more intense laser light. Figure 3.10 shows a region studied under these conditions. It is apparent from these results that the spatial periodicity observed in early SERS measurements of the PPLN/Ag-nanowire system is due to the preferential deposition of SERS-active disordered carbon layers on the positive domains.

Having demonstrated that laser damage effects obscure the enhancement from the wires alone, the effects of laser power and exposure times were examined in order to hopefully avoid photographitization.

SERS intensity was measured as a function of time of exposure to laser radiation and as a function of laser intensity. Laser damage occurred in the silver pyridine system on a time scale of the same order of magnitude as a typical Raman scan (~1 minute). However, for the aqueous benzoic acid system, laser damage occurred much more slowly and enhancement could be monitored as a function of time. Figure 3.11 shows the SERS intensity as a function of time for three different laser powers (25, 50, and 100 mW) each taken at a unique location. An equilibrium is reached for each laser power after approximately 30 minutes, but it can be seen that the enhancement in this system is not linear with laser powers above 50 mW.

This can also be seen in pyridine by measuring enhancement factors at several locations with different laser powers after five minutes of illumination (Figure 3.12). The laser damage caused by laser powers above 50 mW created irreversible damage to the region. It is proposed that the carbon layer can become so thick as to obscure the surface

enhanced signal. Although some authors have explained this difference by suggesting that the carbon-like layer is created at the expense of the adsorbed analyte.[20]

No enhancement is observed on samples for approximately 20 minutes after adding the analyte. This is normally believed to be the time required for the analyte to adsorb to the silver. During this time little to no laser damage is created despite excitation.

3.4 Conclusions

Despite the increased control over the position and shape of the nanoparticles offered by ferroelectric lithography, substrates studied still suffer from lack of reproducibility typical of SERS substrates. Greater attention paid to surface preparation may help to create silver features in a more predictable and repeatable manor.

Several options are proposed for avoiding the laser damage phenomenon which must be achieved in order to study the enhancement of the nanowires alone. Surface carbon Raman peaks are evident in many SERS experiments although few authors use post SERS analysis to check for carbon deposition or laser damage.[21] The chemical process that leads to photographitiaztion is proposed by Cooney et al.[22] The process begins when trace amounts of CO_2 in the aqueous solvent are electroreduced to create HCO_2^- which is adsorbed on the silver along with the analyte. The organic analyte and formate decompose under surface enhanced excitation to form an oxidized graphite layer which can further intercalate the analyte. It is proposed that the carbon-analyte matrix increases the concentration of analyte in the damage region and thus increases the enhancement. Kim et al. established that the carbon layer is not required for surface enhancement by using non-aqueous solvents, it was also noted that the enhancement was greater in systems in which photographitization occurred.[23]

Carbon dioxide's solubility in water makes it a potential contaminant in aqueous solutions. Non-aqueous solvents such as methanol and isopropanol are commonly used in SERS experiments and may help to limit photographitization.[24] Initial measurements with Benzoic acid in isopropanol and pyridine in methanol were difficult to perform due to the

rapid evaporation rate of these solvents. Although SERS has been detected for both solutions on PPLN/Ag-nanowire substrates, the enhancement factors were orders of magnitude smaller than their aqueous counterparts. Enhancement factors were so low that SERS spectra can only be observed at seemingly randomly located hot spots.

Laser damage has also been avoided by using longer wavelength light[25] and even protective monolayers that prevent silver complexation.[26]

Ferroelectric lithographically deposited silver nanostructures could eventually be used by depositing macromolecules (much larger than the nanowires) on the wires in order to exclusively enhance the Raman modes of the part of the molecule near the wire. Because macromolecules have thousands of bonds, their Raman signals are very complex, and being able to isolate certain portions of the molecule for enhancement may enable structure analysis.

References

1) M. Moskovits, in *Surface Enhanced Raman Scattering: Physics and Applications*, edited by K. Kneipp, M. Moskovits, H. Kneipp (Springer-Verlag, Berlin, 2006) p.1.

2) D. Pristinski et al., Journal of Raman Spectroscopy, **37**, 762, (2007).

3) J. A. Creighton, C. G. Blatchford, M. G. Albrecht, Jounal of the Chemical Society-Faraday Transactions II, 75, 790 (1979).

4) G. Mie, Ann. Physik, 25, 377 (1908).

5) W. H. Yang, G. C. Schatz, and R. P. Vandyne, Journal of Chmical Physics, 103, 869 (1995).

6) P. A. Lund, R. R. Smardzewski, and G. E. Tevault, Chemical Physics Letters, 89, 508 (1982).

7) P. F. Liao and M. B. Stern, Optics Letters, 7, 483 (1982).

8) C. Jennings, R. Aroca, A. M. Hor, and R. O. Loutfy, Analytical Chemistry 56, 2033 (1984).

9) D. S. Wang, H. Chew, and M. Kerker, Applied Optics, 19, 2256 (1980).

10) J. Gersten and A. Nitzan, Journal of Chemical Physics, 73, 3023 (1980).

11) O. Sestak, P. Matejka, and B. Vlckova, Collect. Czech. Chem. Commun., 61, 59 (1996).

12) L. Zhao, K. L. Kelly, and G. C. Schatz, J. Phys. Chem. B, 107, 7343 (2003).

13) J.N. Hanson, B.J. Rodriguez, R.J. Nemanich, A. Gruverman, Nanotechnology, **17**, 4946 (2006).

14) S.V. Kalinin and D.A. Bonnell, Phsy. Rev. B, **63**, 125411 (2001).

15) J.G. Scott et al., Appl. Phys. A, **79**, 691 (2004).

16) T. Watanabe, O. Kawanami, K. Honda, Chemical Physics Letters, **102**, 565 (1983).

17) M. R. Mahoney, M.W. Wood, R.P. Cooney, Chem. Phys. Lett., **71**, 59 (1980).

18) T. P. Mernagh, R. P. Cooney, and K. E. Turner, Chemical Physics Letters 110, 536 (1984).

19) A. Nitzan A. and L. E. Brus, Journal of Chemical Physics, 75, 2205 (1981).

20) J.C. Tsang, J.E. Demuth, P.N. Sanda, J.R. Kirtley, Chemical Physics Letters, **76**, 54 (1980).

21) G. Ritchie and C. Y. Chen, in Surface Enhanced Raman Scattering, edited by R. K. Chang and T. E. Furtak (Plenum Press, New York, 1982).

22) R.P. Cooney et al., Chem. Phys. Lett., **79**, 459 (1981).

23) Kim, Chemical Physical Letters, **122**, 139 (1985).

24) M. W. Howard and R. P. Cooney, Chemical Physics Letters, 87, 299 (1982).

25) M. L. McGlashen, U. Guhathakurta, K. L. Davis, and M. D. Morris, Applied Spectroscopy, 45, 543 (1991).

26) E.J. Bjerneld et al., J. Phys. Chem. A, **108**, 4187 (2004).

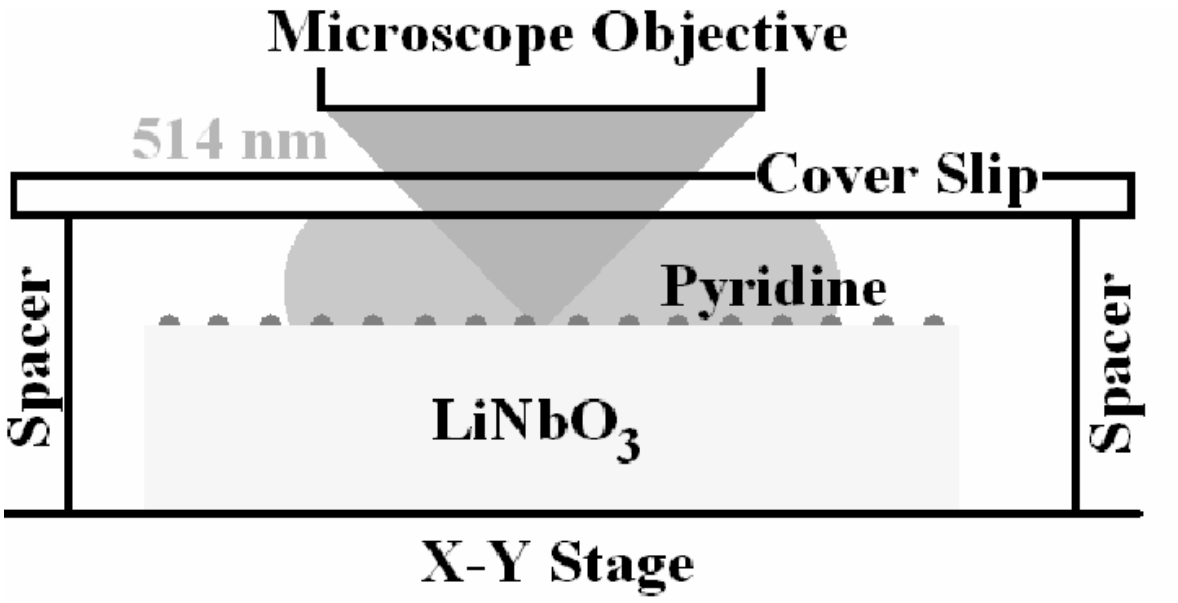

Figure 3.1 Schematic of micro-Raman sampling stage.

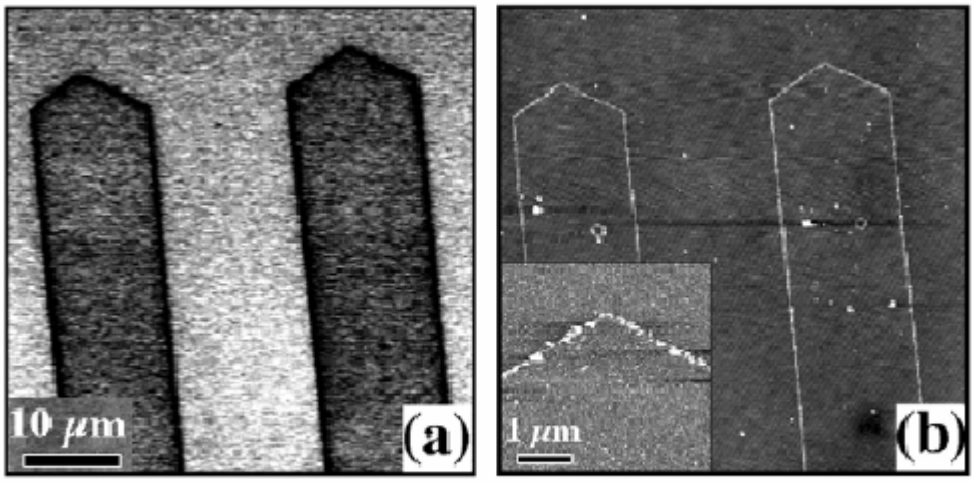

Figure 3.2 AFM and PFM of silver nanowires created by ferroelectric lithography. PFM amplitude Image (a) and AFM topography image (b) of wires created by Ferroelectric Lithography. The dark regions in the phase diagram represent the positive domain.

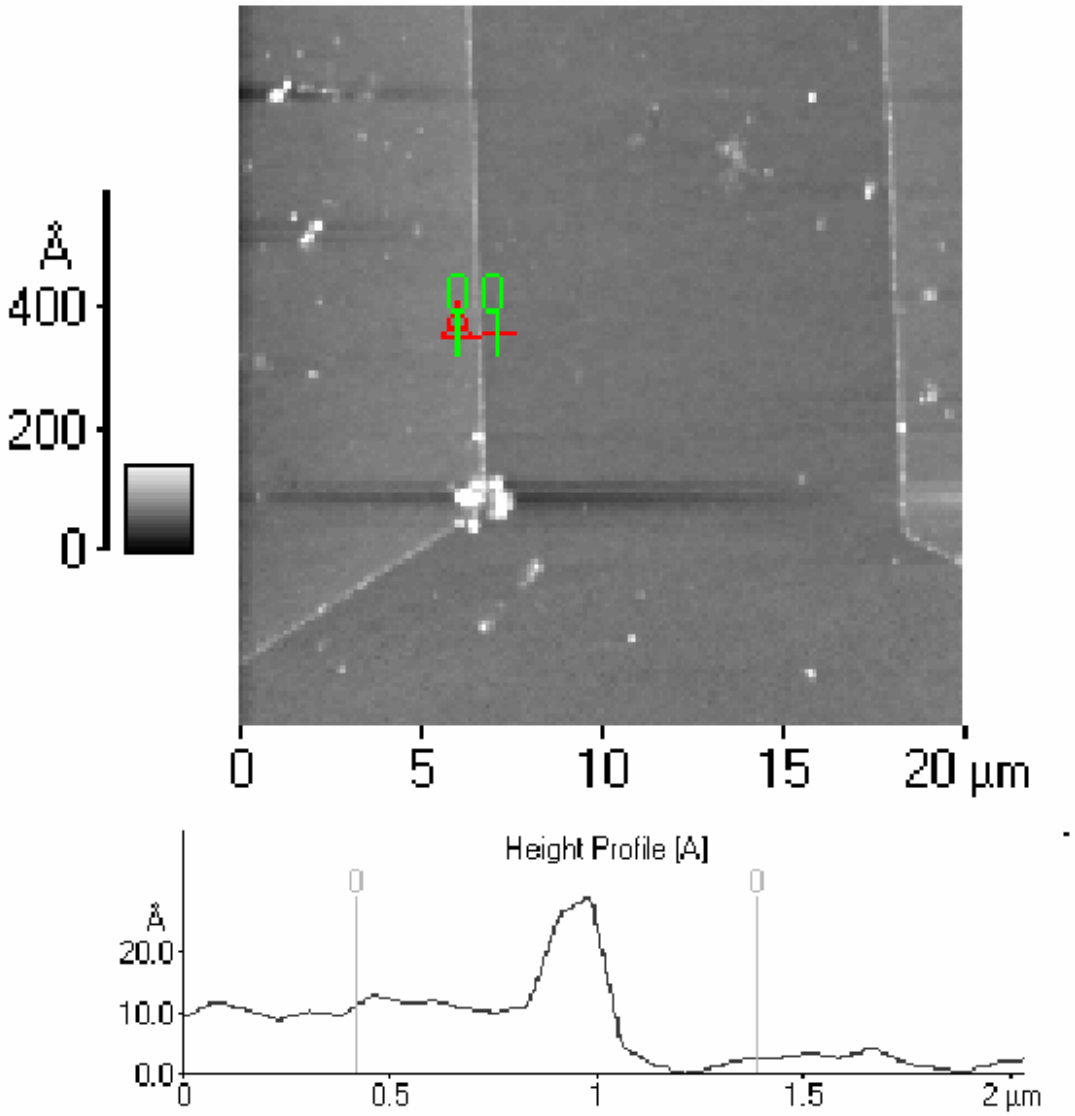

Figure 3.3 AFM height profile of selective deposition on domain boundary and positive domain.
The line scan in the lower image shows that silver is deposited not only on the wire (locate at position equal 1 µm in the lower image) but also on the entire positive domain. The higher domain is known to be the positive domain because of the shape of the domain. The height difference between the two domains is approximately 1 nm.

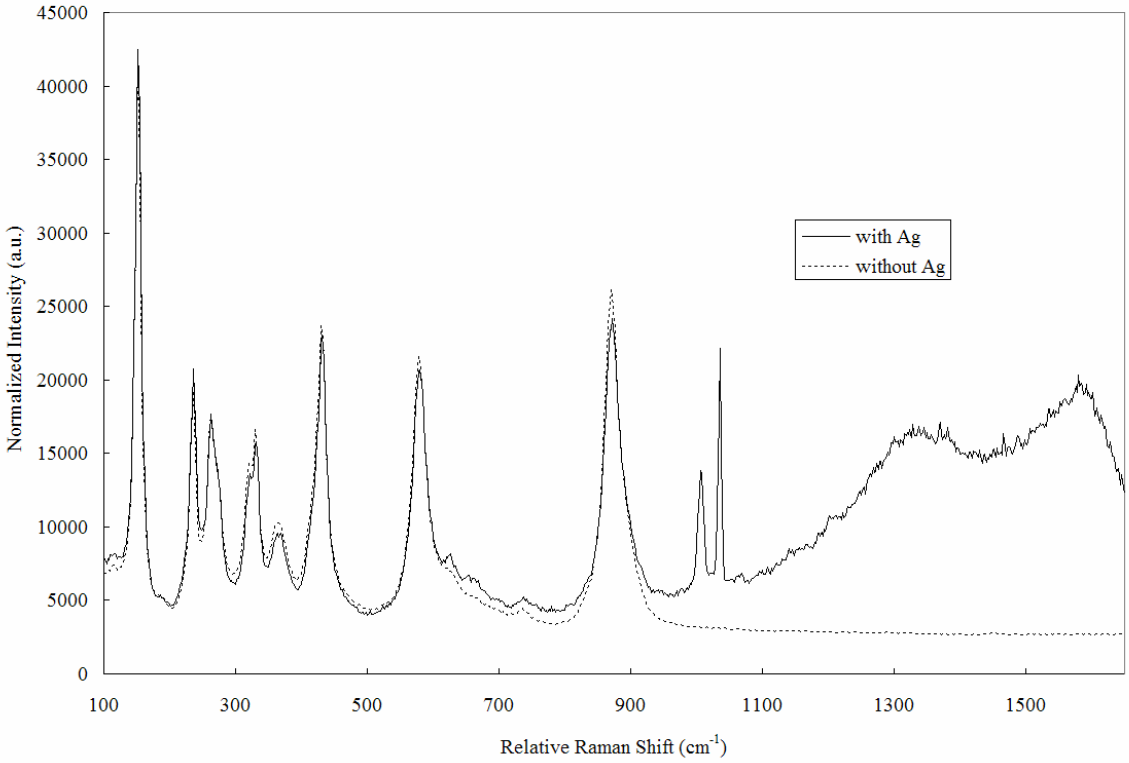

Figure 3.4 SERS of 10^{-4} M pyridine on lithium niobate with and without silver nanowires.
Raman spectra of two lithium niobate samples are shown. Both samples had a drop of 10^{-4} M aqueous pyridine on them, while only one sample (a) had silver nanowires. All peaks below 900 cm^{-1} that are common to both spectra are typical of lithium niobate. The two sharp peaks near 1000 cm^{-1} in (a) are representative of adsorbed pyridine ring breathing modes. The two broad peaks at 1350 and 1580 cm^{-1} in (a) are typical of adsorbed surface carbon.

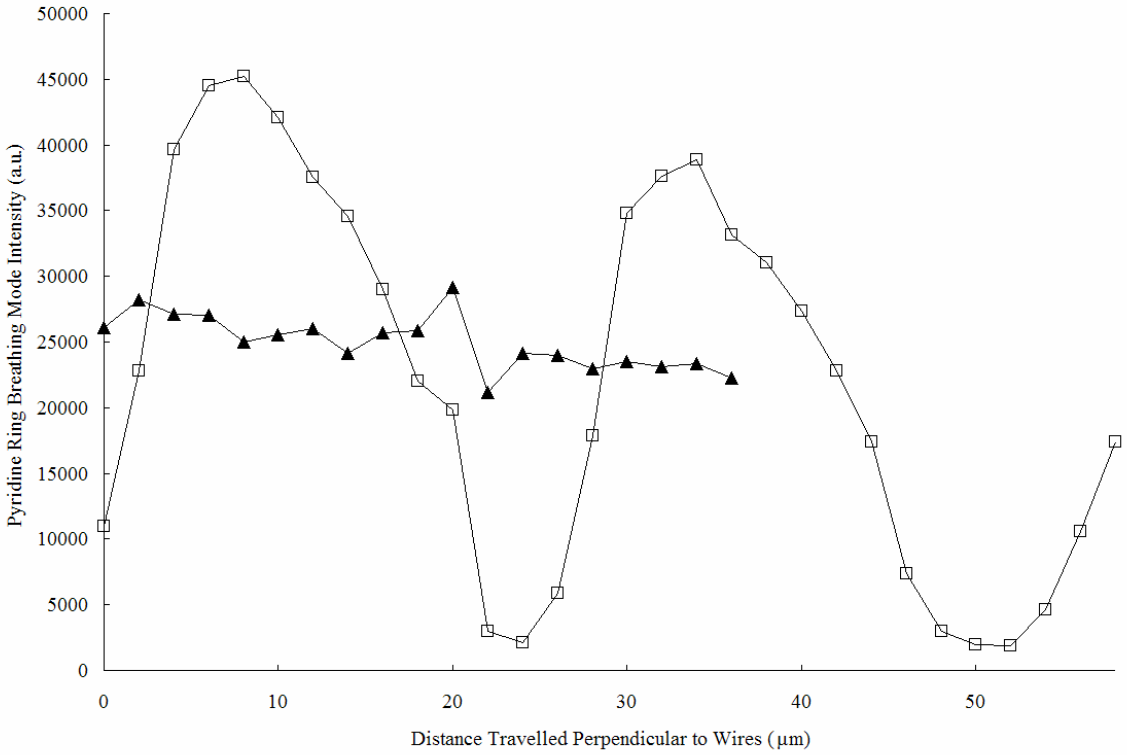

Figure 3.5 Spatially periodic enhancement of pyridine ring breathing mode intensity. Pyridine Ring Breathing mode intensity varies periodically when the laser is scanned in a direction perpendicular to the domains (□). When the laser is scanned in a direction parallel to the domains, the intensity changes slowly (▲).

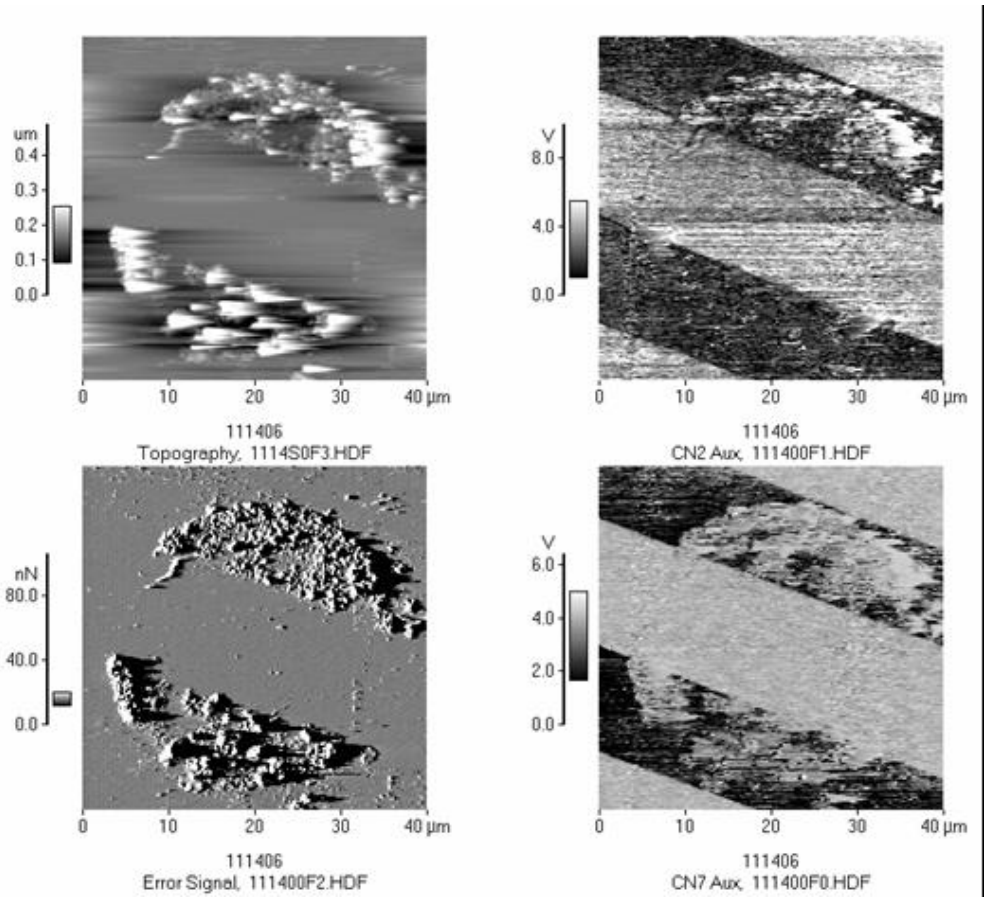

Figure 3.6 AFM and PFM of laser damaged region.
Contact mode AFM topography (top left) and error signal (bottom left) along with PFM amplitude (top right) and phase (bottom right) images show that damage is confined to the positive (dark) domains.

Figure 3.7 SEM of silver nanowires on lithium niobate.
Four SEM images of silver nanowires (3 minute deposition time) are displayed. Dark and bright regions at the top and bottom (respectively) of image (a) are due to charging of the insulating $LiNbO_3$ surface. In (a), three wires can be seen which are 8 and 12 μm apart. (b), (c), and (d) show more detailed images of the wire and occasional silver islands found away from the domain boundary. These islands were not found preferentially on either domain.

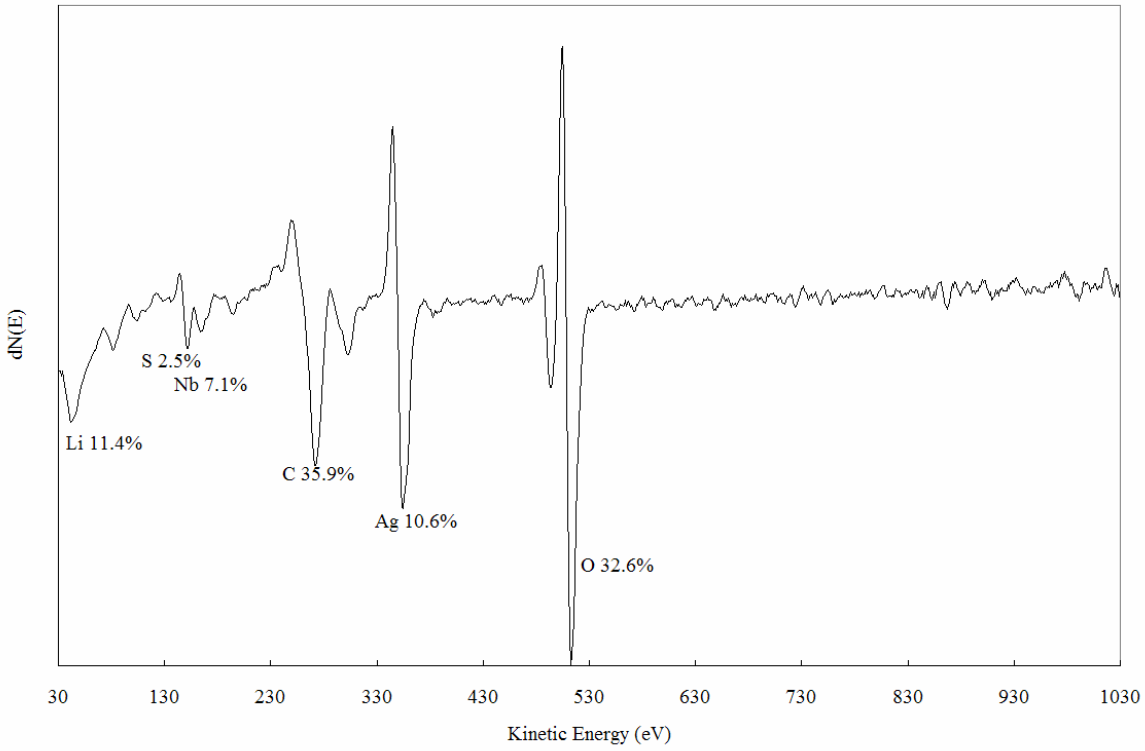

Figure 3.8 Auger spectroscopy of lithium niobate with silver nanowires.

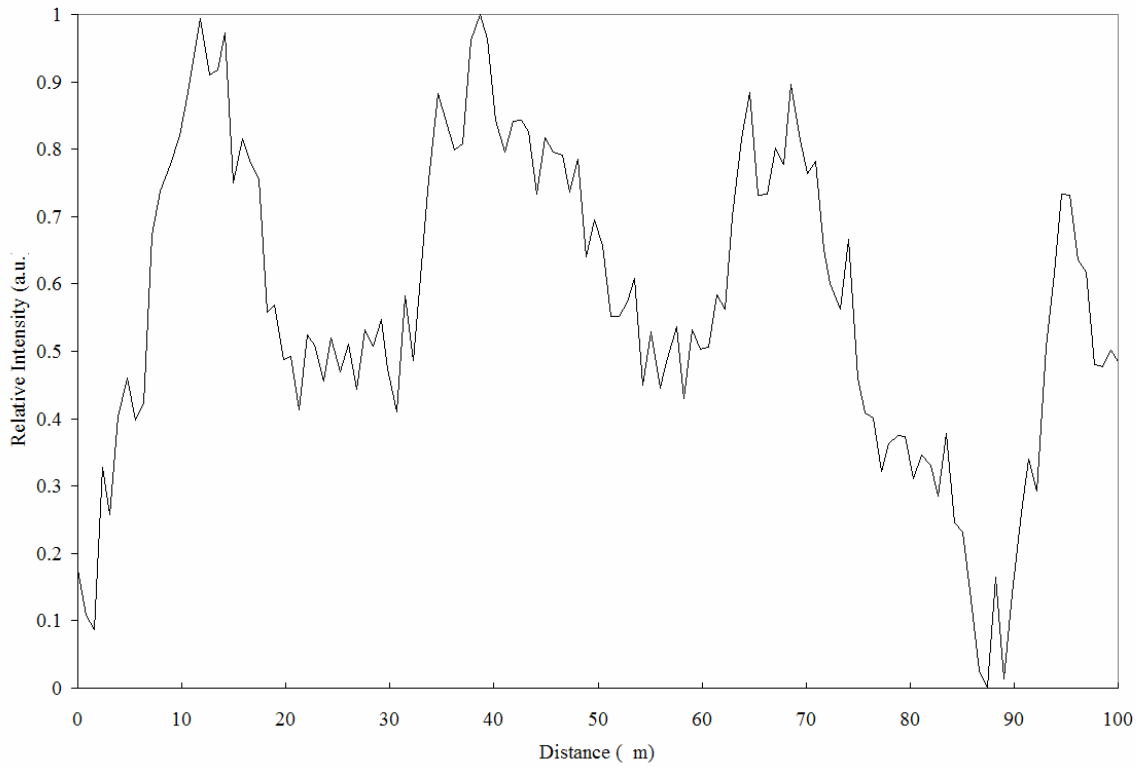

Figure 3.9 Scanning Auger microscopy on silver nanowires on PPLN.

a)

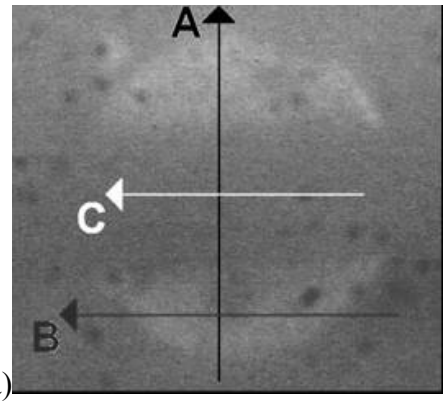

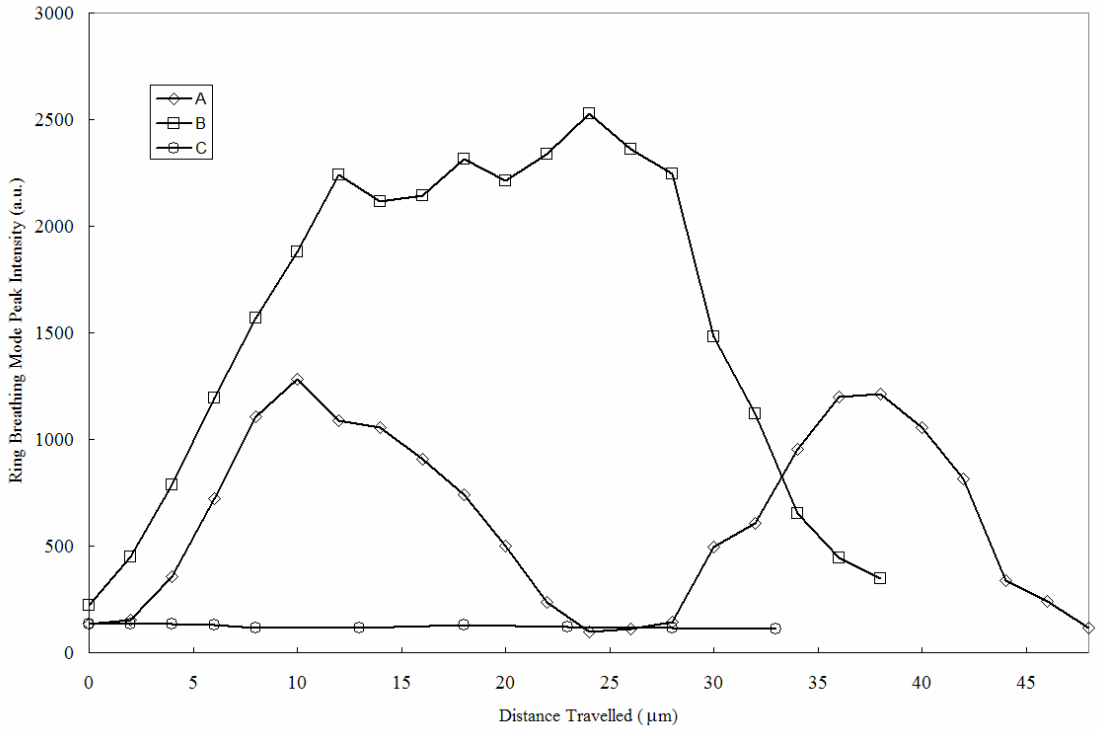

b)

Figure 3.10 SERS of laser damaged region.
Optical Micrograph (a) and SERS (b) of a laser damaged region. Arrows in (a) represent the corresponding SERS intensity in (b).

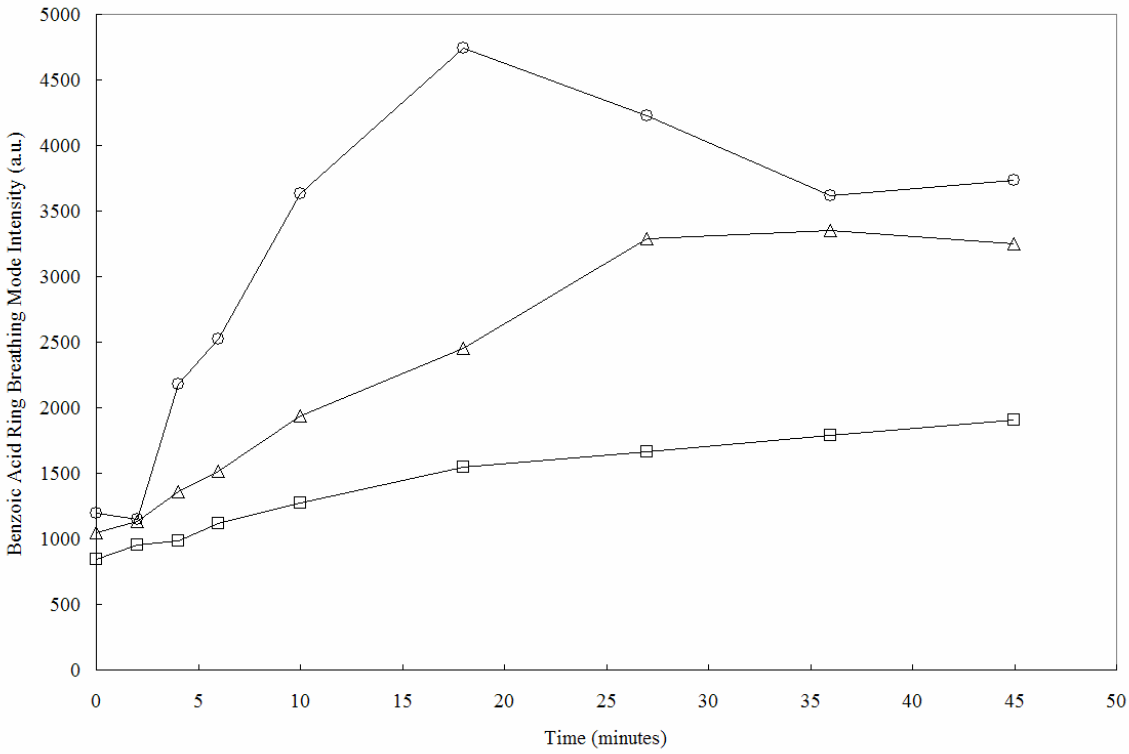

Figure 3.11 Benzoic acid SERS intensity as a function of time.
Benzoic acid ring breathing mode SERS intensities for three laser powers are shown: 25 mW (□), 50 mW (Δ), and 100 mW (○).

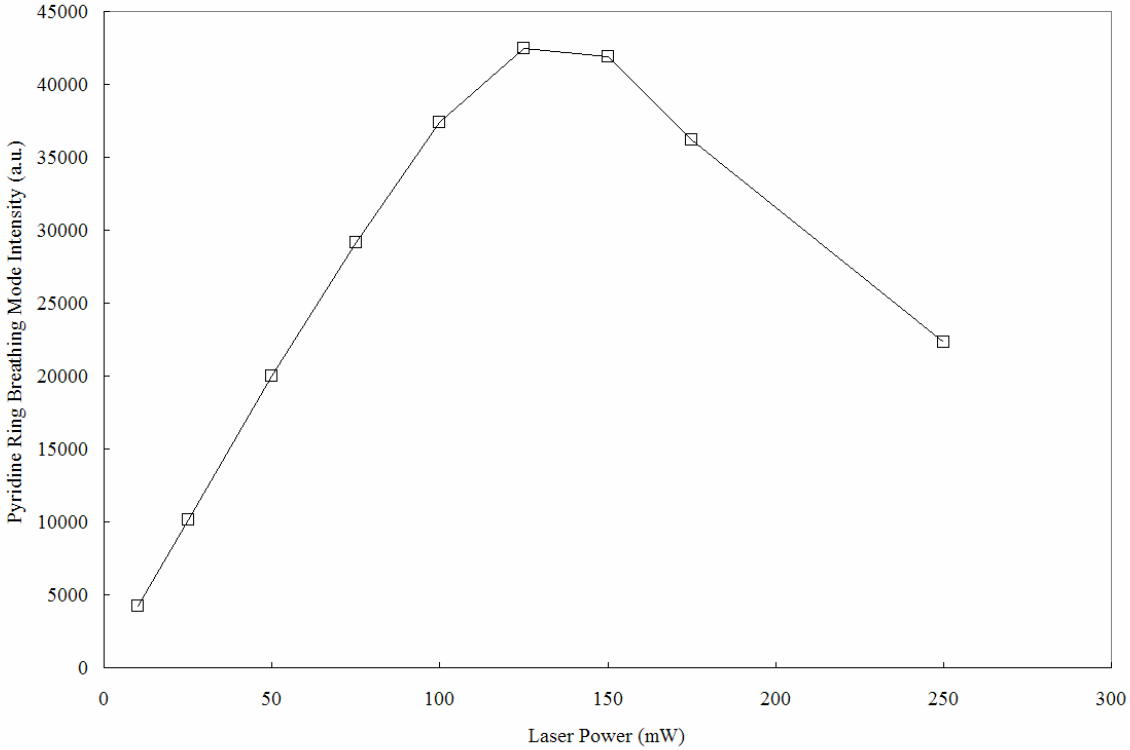

Figure 3.12 Effect of laser power on pyridine SERS intensity.

4. Epilogue

4.1 Ammonothermal Future Work

The Raman spectra of supercritical water and ammonia have been collected with both visible and UV excitation over a temperature and pressure range appropriate for solvothermal growth. Several parameters including hydrogen bonding, Fermi resonance, and pyramidal height, which may affect transport and chemical properties, are monitored by Raman spectroscopy as functions of temperature, pressure, and fill percent. These parameters seem unaffected by the addition of sodium azide. Solutions of sodium azide in ammonia are monitored up to the decomposition temperature. As NaN_3 decomposes to form $NaNH_2$, N_2 and H_2 are also produced. The Raman intensity of the azide decreases at an increasing rate as the reaction proceeds suggesting that the reaction rate increases with pressure. The N_2 Raman signal is also observed to increase during the reaction.

The obvious next step in this work is the inclusion of metallic gallium or powdered GaN feedstock. This will allow detection of the proposed ternary amide intermediates ($Ga(NH_2)_4^-$ or $Ga(NH_2)_5^{2-}$). It has been determined that the intermediate, once formed, is highly soluble at even moderate temperatures making detection likely. Being able to observe the rate of formation and thermodynamic conditions that facilitate not only the formation, but also the precipitation of GaN would be possible. Simulating the dissolution region should be possible with current fill designs, but the crystallization zone is at a much higher temperature (due to the retrograde solubilities of these intermediates). If the window was able to survive higher temperatures, KN_3 mineralizers (which are preferred by

growers due to KNH_2 solubility) could be observed through their decomposition temperature (380 C). Several improvements to the cell will have to be made to make this possible.

The window braze joints are the key weak spot of the cell. Metalization of the sapphire cylinder outer diameter can keep braze material off of the front and back faces of the window and will make this joint stronger. Moving the window all the way to the tip of the housing, or using a different alloy with more compatible thermal expansion coefficient may help increase the temperature ability. There are also fill valves that can handle higher temperatures, this would allow the entire internal volume to be held at a constant temperature and simplify the thermodynamic analyses. There are also types of pressure transducers which are more linear over this temperature range. Adding a port to the cell to place the thermocouple in better thermal contact with the solvent would increase thermodynamic accuracy which is important to perform alongside spectral analysis. Use of a higher quality sapphire can prevent sapphire fluorescence which can obscure Raman data at certain temperatures. An inert internal standard would make intensity comparisons more accurate, but it may be possible to use the sapphire window for this purpose.

4.2 SERS Future Work

A spatially periodic enhancement factor is observed from several analytes adsorbed on silver nanowires grown on PPLN. The enhancement period is equal to the period of the domains not of the wires. Laser damage, caused by photographitization of CO_2 and the organic analytes occurs preferentially on the positive domains because small amounts of silver are deposited there. The carbon laser damage regions are SERS active and obscure enhancement from the wires.

Because periodically poled lithium niobate is relatively expensive, substrates were cleaned and reused for SERS experiments. Even though it was determined by AFM/PFM that the damage caused to the sample for one cleaning cycle was minimal, the surface and wire quality is probably decreased by dozens of cleaning cycles. Surface preparation has been seen to be very important in the silver deposition. Using fresh samples and examining more closely the effects of surface preparation on wire growth are the most important next step. Samples made using the same deposition conditions can show islands, whole domain coverage, or only wires.

Deposition at elevated temperature showed better wire quality on stoichiometric LN. Stoichiometric LN also allows for custom domain patterning, but SLN is much more expensive than the congruent counterparts used in this study.

Because low laser powers did not cause laser damage, they could be used to perform SERS analysis if the system throughput could be increased or if an analyte with

higher scattering cross section could be increased. Several other methods for avoiding laser damage include non-aqueous solvents, protective layers, and longer wavelength excitation.